

Review

# [<sup>18</sup>F]Fluspidine—A PET Tracer for Imaging of $\sigma_1$ Receptors in the Central Nervous System

Friedrich-Alexander Ludwig<sup>1</sup>, Erik Laurini<sup>2</sup>, Judith Schmidt<sup>3</sup>, Sabrina Priel<sup>2,4</sup>, Winnie Deuther-Conrad<sup>1</sup>  
and Bernhard Wunsch<sup>3,5,\*</sup>

- <sup>1</sup> Institute of Radiopharmaceutical Cancer Research, Department of Neuroradiopharmaceuticals, Helmholtz-Zentrum Dresden-Rossendorf, D-04318 Leipzig, Germany; f.ludwig@hzdr.de (F.-A.L.); w.deuther-conrad@hzdr.de (W.D.-C.)
  - <sup>2</sup> Molecular Biology and Nanotechnology Laboratory (MolBNL@UniTS), DEA, University of Trieste, 34127 Trieste, Italy; erik.laurini@dia.units.it (E.L.); sabrina.priel@dia.units.it (S.P.)
  - <sup>3</sup> Institut für Pharmazeutische und Medizinische Chemie, Universität Münster, Corrensstraße 48, D-48149 Münster, Germany; judith.schmidt7@uni-muenster.de
  - <sup>4</sup> Department of General Biophysics, Faculty of Biology and Environmental Protection, University of Lodz, 90-136 Lodz, Poland
  - <sup>5</sup> GRK 2515, Chemical Biology of Ion Channels (Chembion), Universität Münster, Corrensstraße 48, D-48149 Münster, Germany
- \* Correspondence: wunsch@uni-muenster.de; Tel.: +49-251-8333311; Fax: +49-251-8332144

**Abstract:**  $\sigma_1$  receptors play a crucial role in various neurological and neurodegenerative diseases including pain, psychosis, Alzheimer's disease, and depression. Spirocyclic piperidines represent a promising class of potent  $\sigma_1$  receptor ligands. The relationship between structural modifications and  $\sigma_1$  receptor affinity and selectivity over  $\sigma_2$  receptors led to the 2-fluoroethyl derivative fluspidine (**2**,  $K_i = 0.59$  nM). Enantiomerically pure (*S*)-configured fluspidine ((*S*)-**2**) was prepared by the enantioselective reduction of the  $\alpha,\beta$ -unsaturated ester **23** with NaBH<sub>4</sub> and the enantiomerically pure co-catalyst (*S,S*)-**24**. The pharmacokinetic properties of both fluspidine enantiomers (*R*)-**2** and (*S*)-**2** were analyzed in vitro. Molecular dynamics simulations revealed very similar interactions of both fluspidine enantiomers with the  $\sigma_1$  receptor protein, with a strong ionic interaction between the protonated amino moiety of the piperidine ring and the COO<sup>−</sup> moiety of glutamate 172. The <sup>18</sup>F-labeled radiotracers (*S*)-[<sup>18</sup>F]**2** and (*R*)-[<sup>18</sup>F]**2** were synthesized in automated syntheses using a TRACERlab FX FN synthesis module. High radiochemical yields and radiochemical purity were achieved. Radiometabolites were not found in the brains of mice, piglets, and rhesus monkeys. While both enantiomers revealed similar initial brain uptake, the slow washout of (*R*)-[<sup>18</sup>F]**2** indicated a kind of irreversible binding. In the first clinical trial, (*S*)-[<sup>18</sup>F]**2** was used to visualize  $\sigma_1$  receptors in the brains of patients with major depressive disorder (MDD). This study revealed an increased density of  $\sigma_1$  receptors in cortico-striato-(para)limbic brain regions of MDD patients. The increased density of  $\sigma_1$  receptors correlated with the severity of the depressive symptoms. In an occupancy study with the PET tracer (*S*)-[<sup>18</sup>F]**2**, the selective binding of pridopidine at  $\sigma_1$  receptors in the brain of healthy volunteers and HD patients was shown.

**Keywords:**  $\sigma_1$  receptor ligands;  $\sigma_1:\sigma_2$  selectivity; structure–affinity relationships; enantioselective synthesis; pharmacokinetics; logD<sub>7.4</sub> value; plasma protein binding; biotransformation; molecular dynamics simulations; ligand– $\sigma_1$  receptor interactions; radiosynthesis; automated radiosynthesis; radiometabolites; biodistribution; irreversible binding of (*R*)-[<sup>18</sup>F]**2**; major depressive disorder; increased  $\sigma_1$  receptor density; occupancy study with pridopidine



**Citation:** Ludwig, F.-A.; Laurini, E.; Schmidt, J.; Priel, S.; Deuther-Conrad, W.; Wunsch, B. [<sup>18</sup>F]Fluspidine—A PET Tracer for Imaging of  $\sigma_1$  Receptors in the Central Nervous System. *Pharmaceuticals* **2024**, *17*, 166. <https://doi.org/10.3390/ph17020166>

Academic Editors: Giorgio Treglia, Katarzyna Szczepanska and Katarzyna Kiec-Kononowicz

Received: 12 December 2023

Revised: 18 January 2024

Accepted: 25 January 2024

Published: 28 January 2024



**Copyright:** © 2024 by the authors. Licensee MDPI, Basel, Switzerland. This article is an open access article distributed under the terms and conditions of the Creative Commons Attribution (CC BY) license (<https://creativecommons.org/licenses/by/4.0/>).

## 1. Introduction: The Role of $\sigma_1$ Receptors in Some Brain Diseases

The  $\sigma_1$  receptor is highly expressed in the central nervous system (CNS) and therefore is centrally involved in various pathological conditions of the CNS. Therefore, the labeling

of  $\sigma_1$  receptors with a positron emission tomography (PET) tracer, allowing non-invasive imaging, represents a valuable tool for target validation as well as diagnosis and prognosis. In this report, we will focus on the participation of the  $\sigma_1$  receptor in pain, psychosis, Alzheimer's disease, and depression [1–3].

### 1.1. Pain

A functional connection between the  $\sigma_1$  and opioid receptor systems has been reported. The downregulation of the  $\sigma_1$  receptor led to an increased analgesic activity of opioid analgesics [2]. The same effect could be produced by  $\sigma_1$  receptor antagonists such as haloperidol (Figure 1). On the other hand,  $\sigma_1$  receptor agonists (e.g., (+)-pentazocine, Figure 1) resulted in reduced analgesia mediated by opioid (MOR) agonists [4]. However,  $\sigma_1$  receptors are also directly involved in pain sensation, in particular in the special type of neuropathic pain. While capsaicin produced mechanical allodynia in wild-type mice, it failed to induce the same effect in  $\sigma_1$  receptor knock-out mice. Furthermore,  $\sigma_1$  receptor antagonists could dose-dependently reduce capsaicin-mediated mechanical allodynia, while  $\sigma_1$  receptor agonists reversed this analgesic effect [5]. The  $\sigma_1$  receptor antagonist S1RA (Figure 1) represents the most advanced drug candidate, exhibiting high analgesic activity in animal models of neuropathic pain. S1RA is currently being investigated in a phase II clinical trial for the treatment of neuropathic pain [6,7].

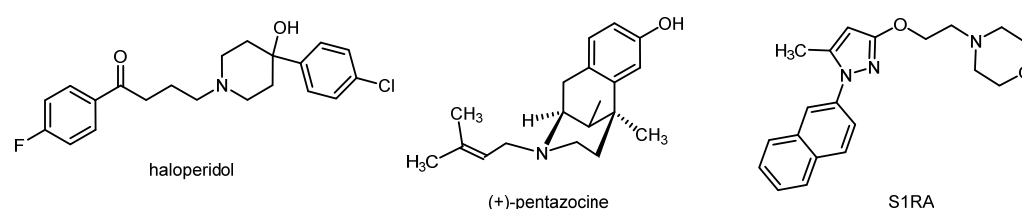


**Figure 1.**  $\sigma_1$  receptor ligands modulating pain perception. The  $\sigma_1$  receptor antagonist S1RA is active in the treatment of neuropathic pain.

### 1.2. Psychosis

Classical antipsychotics inhibit the G protein-coupled dopamine  $D_2$  receptor. However, the prototypical antipsychotic haloperidol (Figure 1) inhibits not only  $D_2$  receptors (binding affinity:  $K_i(D_2) = 2.6$  nM) [8], but also  $\sigma_1$  receptors with high affinity ( $K_i(\sigma_1) = 6.2$  nM) [9]. Other clinically used antipsychotics (e.g., chlorpromazine as a member of the class of phenothiazines, Figure 2) also show moderate to high  $\sigma_1$  receptor affinity [10]. It was hypothesized that the inhibition of  $\sigma_1$  receptors is capable of contributing to the overall antipsychotic effects of these  $D_2$  receptor antagonists [11]. In addition to these “mixed  $D_2/\sigma_1$  receptor antagonists”, some ligands predominantly inhibiting  $\sigma_1$  receptors (e.g., eliprodil (SL82.0715), rimcazole (BW234U), panamesine (EMD57445), DuP734, and BMY14802 (BMS181100)) were tested in clinical trials for their potential use as antipsychotics. In Figure 2, the structures of eliprodil, rimcazole, and panamesine are shown, exemplarily [12].

### 1.3. Alzheimer's Disease

The  $\sigma_1$  receptor agonist (+)-pentazocine was able to attenuate the memory deficits in mice treated with amyloid  $\beta_{25-35}$  (cerebroventricular application) in a dose-dependent mode. In animal models of Alzheimer's disease (chronic intracerebroventricular infusion of the amyloid  $\beta_{1-40}$  protein),  $\sigma_1$  receptor agonists improved depressive behavior in mice [13,14]. The acetylcholinesterase inhibitor donepezil (Figure 3) is one of the first-line drugs used for the treatment of Alzheimer's disease. In addition to the inhibition of acetylcholinesterase, donepezil can also activate  $\sigma_1$  receptors. It was hypothesized that the activation of  $\sigma_1$  receptors by donepezil contributes to its neuroprotective and anti-amnesic effects [15]. In PET studies, a low  $\sigma_1$  receptor density was found for patients at an early stage of Alzheimer's disease [16].

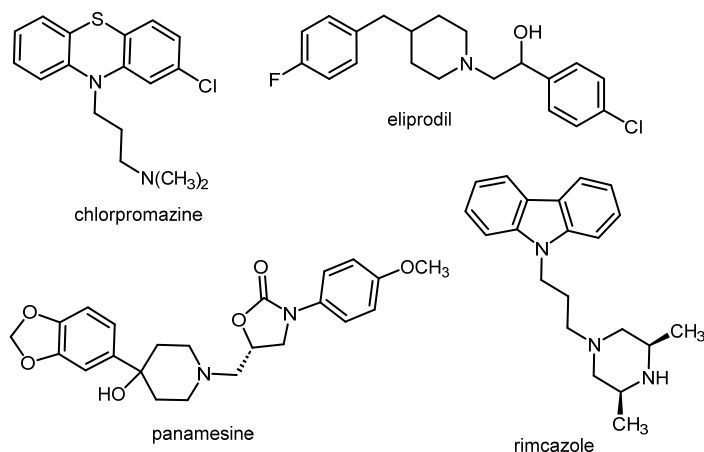


**Figure 2.**  $\sigma_1$  receptor antagonists with antipsychotic potential.

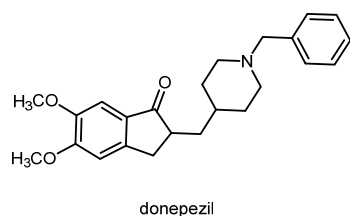


**Figure 3.** Donepezil, an acetylcholinesterase inhibitor and  $\sigma_1$  receptor agonist used for the treatment of Alzheimer's disease.

#### 1.4. Depression

Various studies have shown that  $\sigma_1$  receptors are involved in the pathology of depression. A depressive-like behavior was observed in  $\sigma_1$  receptor knock-out mice [17]. In the forced swimming test, which is used to evaluate antidepressant drugs, some  $\sigma_1$  receptor agonists exhibited antidepressant activity [18,19]. Furthermore, several clinically used antidepressants, such as tricyclic antidepressants and selective serotonin reuptake inhibitors (SSRIs), show moderate to high  $\sigma_1$  receptor affinity. Figure 4 displays imipramine and opipramol as examples of the class of tricyclic antidepressants, and fluoxetine, fluvoxamine, and sertraline as examples of SSRIs. The repeated treatment of rats with the antidepressants imipramine and fluvoxamine, but also with the  $\sigma_1$  receptor agonist (+)-pentazocine, led to the downregulation of  $\sigma_1$  receptors in some regions of the brain, including the striatum, hippocampus, and cerebral cortex [20,21].

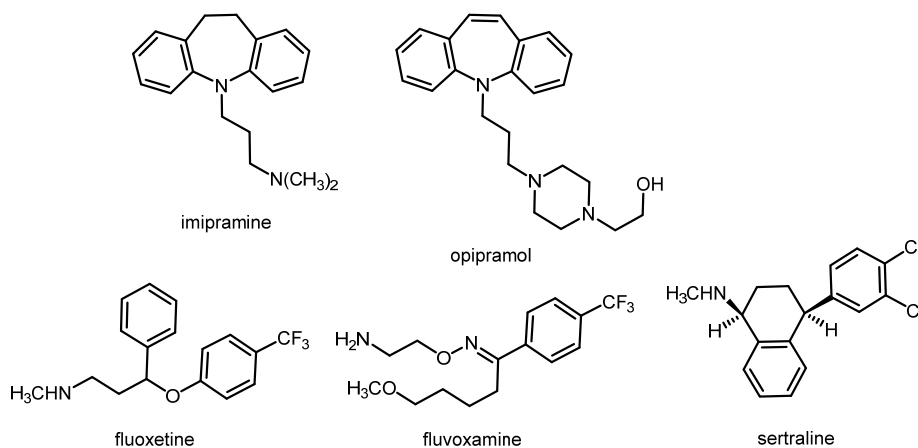


**Figure 4.** Clinically used antidepressants with  $\sigma_1$  receptor agonistic activity.

## 2. Fluorinated PET Tracers Derived from the Promising $\sigma_1$ Ligand Cutamesine (SA 4503)

The introduction of fluorine-18 into an aromatic ring requires the careful selection of appropriate precursors and longer reaction sequences. The introduction of fluorine-18 into aliphatic side chains by  $S_N2$ -substitution is straightforward. However, aryl fluorides are usually rather stable in vivo, while alkyl fluorides carry the risk of defluorination, which would result in bone labeling via the formation of  $[^{18}\text{F}]\text{CaF}_2$ . Several PET tracers bearing aromatic and aliphatic fluorine-18 have been reported in the literature [16,22,23].

The most prominent fluorinated  $\sigma_1$  receptor-targeting PET tracers are derived from the  $\sigma_1$  receptor agonist cutamesine (SA 4503, Figure 5) [24]. Cutamesine has anti-amnesic activity and can reduce amnesia caused by REM sleep deprivation [25,26]. Furthermore, this  $\sigma_1$  receptor agonist showed antidepressant activity in the forced swimming test of rodents [27].

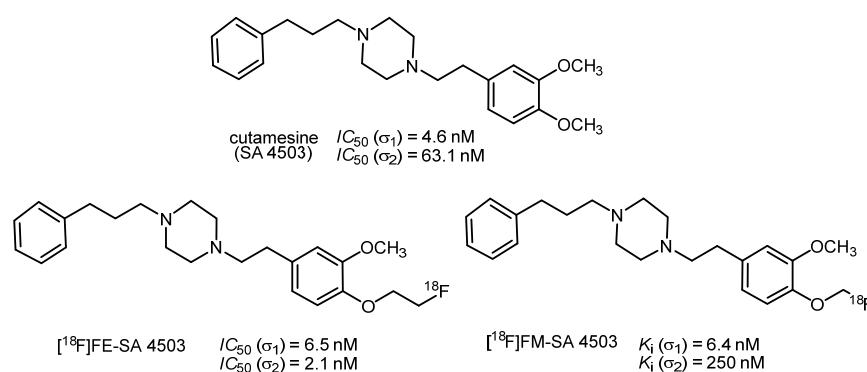


**Figure 5.**  $\sigma_1$  Receptor agonist cutamesine (SA 4503) and derived 18-F-labeled PET tracers  $[^{18}\text{F}]\text{FE-SA 4503}$  and  $[^{18}\text{F}]\text{FM-SA 4503}$ .

The fluoroethyl derivative FE-SA 4503 showed only moderate to low selectivity for the  $\sigma_1$  receptor over the  $\sigma_2$  subtype. In a PET study with rhesus monkeys,  $[^{18}\text{F}]\text{FE-SA 4503}$  exhibited fast uptake in the brain and enrichment in regions with high expression of  $\sigma_1$  receptors. However, an equilibrium of ligand binding to the  $\sigma_1$  receptor was not reached within 90 min [28]. Despite its  $\alpha$ -fluoro ether substructure, the fluoromethyl derivative FM-SA 4503 displayed an unexpectedly high chemical stability in vitro and in vivo. The replacement of  $[^{18}\text{F}]\text{FM-SA 4503}$  with haloperidol in a study with rhesus monkeys revealed a higher specific binding of  $[^{18}\text{F}]\text{FM-SA 4503}$  than of  $[^{11}\text{C}]\text{SA 4503}$ . Although  $[^{18}\text{F}]\text{FM-SA 4503}$  has an unconventional structure, it represents a promising fluorinated PET tracer for the labeling of  $\sigma_1$  receptors in the brain [29].

The  $^{18}\text{F}$ -labeled PET-tracers  $[^{18}\text{F}]\text{FE-SA 4503}$  and  $[^{18}\text{F}]\text{FM-SA 4503}$  (Figure 5) were synthesized in two-step sequences. At first, the  $^{18}\text{F}$ -labeled reagents  $[^{18}\text{F}]\text{FCH}_2\text{CH}_2\text{OTs}$  and  $[^{18}\text{F}]\text{CH}_2\text{BrF}$  were prepared by the nucleophilic substitution of  $\text{TsOCH}_2\text{CH}_2\text{OTs}$  and  $\text{H}_2\text{CBr}_2$ , respectively, with the  $\text{K}[^{18}\text{F}]\text{F}/\text{Kryptofix}$  system. In the second step, the phenolate precursor was reacted with  $[^{18}\text{F}]\text{FCH}_2\text{CH}_2\text{OTs}$  and  $[^{18}\text{F}]\text{H}_2\text{CBrF}$  to afford the  $^{18}\text{F}$ -labeled PET tracers  $[^{18}\text{F}]\text{FE SA4503}$  and  $[^{18}\text{F}]\text{FM SA4503}$ , respectively [28,29].

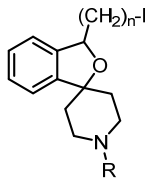
## 3. Spirocyclic $\sigma_1$ Receptor Ligands Designed for PET Studies: Structure Affinity Relationships

We are particularly interested in drugs with a large number of  $\text{sp}^3$ -hybridized C-atoms incorporated in rigid scaffolds, such as spirocyclic, bicyclic, or propellane systems leading to defined three-dimensional frameworks with an exact orientation of functional groups and substituents. Therefore, we started to exploit the pharmacological potential, in particular the  $\sigma_1$  receptor affinity and selectivity, of spirocyclic piperidines.

A homologous series of fluoroalkyl-substituted spirocyclic piperidines **1–4** bearing a benzyl moiety at the piperidine N-atom was prepared. The four homologs **1–4** showed very high  $\sigma_1$  receptor affinities ( $K_i = 0.59\text{--}1.4 \text{ nM}$ ) and low  $\sigma_2$  receptor affinity ( $K_i = 489\text{--}837 \text{ nM}$ ),

resulting in a high  $\sigma_1:\sigma_2$  selectivity [30–34]. The highest  $\sigma_1$  receptor affinity and  $\sigma_1:\sigma_2$  selectivity were observed for the fluoroethyl derivative **2** (Table 1). Therefore, the benzyl moiety of **2** was replaced by several other substituents including substituted benzyl, cyclohexylmethyl, and alkyl moieties. With the exception of the very lipophilic *n*-butyl and *n*-octyl derivatives **8** and **9**, the modified spirocyclic piperidines **5–7** and **10** displayed high  $\sigma_1$  receptor affinity, but reduced selectivity over the  $\sigma_2$  receptor. In particular, the cyclohexylmethyl derivative **6** binds with subnanomolar affinity at  $\sigma_1$  receptors ( $K_i = 0.71$  nM), but also with moderate affinity at  $\sigma_2$  receptors ( $K_i = 57$  nM), leading to a low  $\sigma_1:\sigma_2$  selectivity [31]. The very high  $\sigma_1$  receptor affinity ( $K_i = 0.59$  nM) and  $\sigma_1:\sigma_2$  selectivity (1331-fold) and the promising physicochemical properties (see Chapter 5) prompted us to further develop the fluoroethyl derivative **2**, which was termed fluspidine.

**Table 1.** Spirocyclic piperidines with fluoroalkyl side chains.



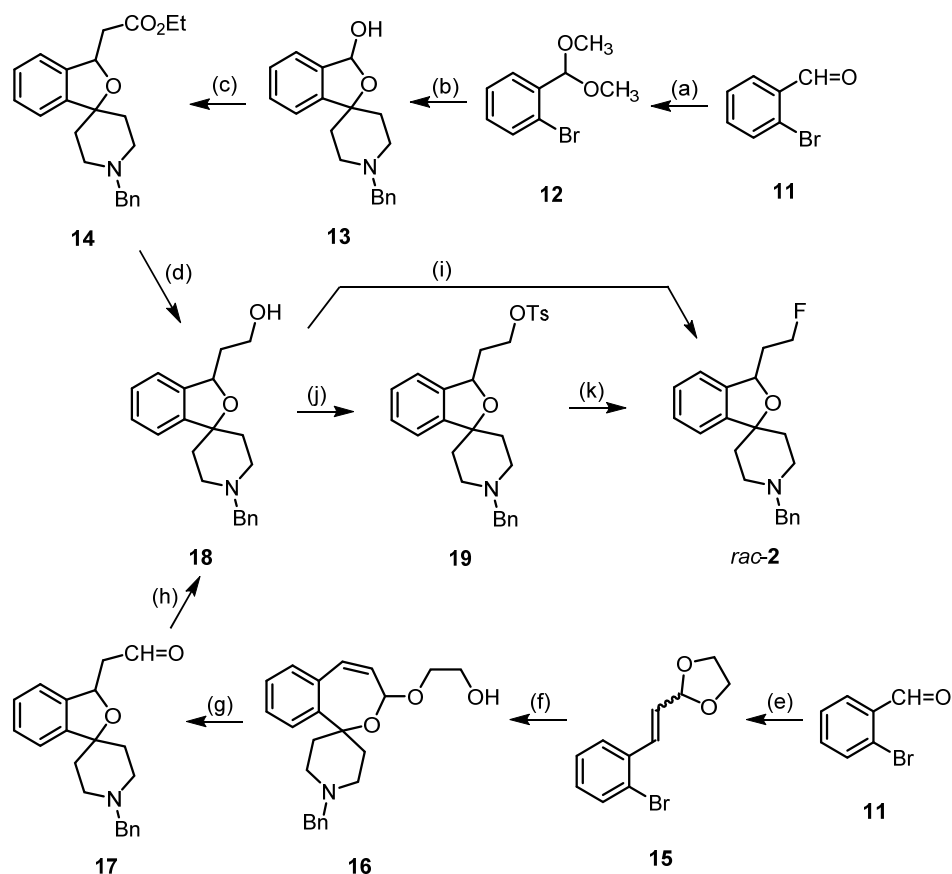
**1-10**

Compd.	<i>n</i>	R	$K_i(\sigma_1)$ (nM)	$K_i(\sigma_2)$ (nM)	$\sigma_1/\sigma_2$ Selectivity
<b>1</b>	1	-CH <sub>2</sub> C <sub>6</sub> H <sub>5</sub>	0.74	550	743
<b>2</b>	2	-CH <sub>2</sub> C <sub>6</sub> H <sub>5</sub>	0.59	785	1331
<b>3</b>	3	-CH <sub>2</sub> C <sub>6</sub> H <sub>5</sub>	1.4	837	598
<b>4</b>	4	-CH <sub>2</sub> C <sub>6</sub> H <sub>5</sub>	1.2	489	408
<b>5</b>	2	-CH <sub>2</sub> C <sub>6</sub> H <sub>4</sub> - <i>p</i> -F	0.57	481	844
<b>6</b>	2	-CH <sub>2</sub> C <sub>6</sub> H <sub>11</sub>	0.71	57	80
<b>7</b>	2	-CH(CH <sub>3</sub> )C <sub>6</sub> H <sub>5</sub>	1.0	>1 $\mu$ M	>1000
<b>8</b>	2	<i>n</i> -butyl	3.9	878	225
<b>9</b>	2	<i>n</i> -octyl	15	118	7.9
<b>10</b>	2	-CH <sub>2</sub> CH=C(CH <sub>3</sub> ) <sub>2</sub>	1.5	>1 $\mu$ M	667

#### 4. Synthesis of Racemic and Enantiomerically Pure Fluspidine (**2**, (*S*)-**2** and (*R*)-**2**)

For the synthesis of racemic fluspidine (**2**), two synthetic routes were pursued, both of which started with 2-bromobenzaldehyde (**11**) (Scheme 1). After the conversion of aldehyde **11** into dimethyl acetal **12**, bromine–lithium exchange with *n*-BuLi led to an aryllithium intermediate, which reacted with 1-benzylpiperidin-4-one to provide the cyclic hemiacetal **13** after hydrolysis with HCl. The Domino reaction of the hemiacetal **13** with the Wittig reagent Ph<sub>3</sub>P=CHCO<sub>2</sub>Et consisted in the opening of the hemiacetal to form an hydroxy aldehyde, the Wittig reaction of the aldehyde to give an  $\alpha,\beta$ -unsaturated ester, and finally an intramolecular Michael addition of the tertiary alcohol to the  $\alpha,\beta$ -unsaturated ester to end up with the spirocyclic ester **14**. The LiAlH<sub>4</sub> reduction of the ester **14** provided the primary alcohol **18** [35].

According to the second route, the Wittig reaction of aldehyde **11** was first performed, leading to the  $\alpha,\beta$ -unsaturated acetal **15**. Bromine–lithium exchange followed by reaction with 1-benzylpiperidin-4-one provided the spirocyclic 2-benzoxepine **16**, which upon hydrolysis with HCl led to ring contraction, giving the (2-benzofuranyl)acetaldehyde **17**. Aldehyde **17** was reduced with NaBH<sub>4</sub> to give the primary alcohol **18** [31] (Scheme 1).



**Scheme 1.** Synthesis of racemic fluspidine *rac-2*. Reagents and reaction conditions: (a)  $\text{CH}_3\text{OH}$ ,  $\text{HC}(\text{OCH}_3)_3$ ,  $\text{TsOH}$ , reflux, 85%. (b) 1. *n*-BuLi,  $-95^\circ\text{C}$ ; 2. 1-benzylpiperidin-4-one,  $-95^\circ\text{C}$ , then rt; 3. HCl, THF,  $66^\circ\text{C}$ , 11%. (c)  $\text{Ph}_3\text{P}=\text{CHCO}_2\text{Et}$ ,  $\text{Cs}_2\text{CO}_3$ , toluene, reflux, 88%. (d)  $\text{LiAlH}_4$ ,  $\text{Et}_2\text{O}$ ,  $-15^\circ\text{C}$ , 75%. (e) [(1,3-dioxolan-2-yl)methyl]triphenylphosphonium bromide [ $(\text{CH}_2\text{O})_2\text{CHCH}_2\text{PPh}_3\text{Br}$ ],  $\text{K}_2\text{CO}_3$ , TDA-1 [tris(methoxyethoxyethyl)amine, 95%]; (f) *n*-BuLi,  $-78^\circ\text{C}$ , then addition of 1-benzylpiperidin-4-one,  $-78^\circ\text{C}$ , then rt, 67%. (g) HCl, 2 M, 37%. (h)  $\text{NaBH}_4$ ,  $\text{CH}_3\text{CN}$ , 37%. (i) DAST,  $\text{CH}_2\text{Cl}_2$ ,  $-78^\circ\text{C}$ , then rt, 56%. (j) TsCl, DMAP,  $\text{NEt}_3$ ,  $\text{CH}_2\text{Cl}_2$ , 17 h, rt, 36%. (k)  $\text{Bu}_4\text{NF}$ , THF, 4 h, rt, 80%.

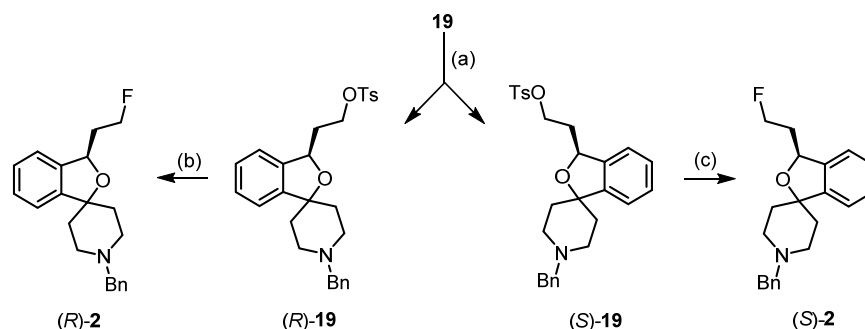
The fluorinating reagent DAST (diethylaminosulfur trifluoride,  $\text{Et}_2\text{NSF}_3$ ) converted the intermediate primary alcohol **18** directly into the fluoroethyl derivative **2** [31]. To prepare the radiosynthesis, the primary alcohol **18** was transformed into the tosylate **19**, which reacted with TBAF (tetrabutylammonium fluoride,  $\text{Bu}_4\text{N}^+\text{F}^-$ ) to produce fluspidine (**2**) [36] (Scheme 1).

In order to obtain pure fluspidine enantiomers (*R*)-**2** and (*S*)-**2**, the chiral resolution of racemic tosylate **19** was conducted. The enantiomeric tosylates (*R*)-**19** and (*S*)-**19** were separated using the Daicel<sup>®</sup> Chiralpak IB column and the eluent isohexane:ethanol 100:2, and the absolute configuration of the enantiomers was determined by CD spectroscopy. Both enantiomers, (*R*)-**19** and (*S*)-**19**, were converted into the fluspidine enantiomers (*R*)-**2** (99.6%ee) and (*S*)-**2** (96.4%ee) using TBAF ( $\text{Bu}_4\text{NF}$ ) as a fluoride source for the  $\text{S}_{\text{N}}2$  substitution [36] (Scheme 2).

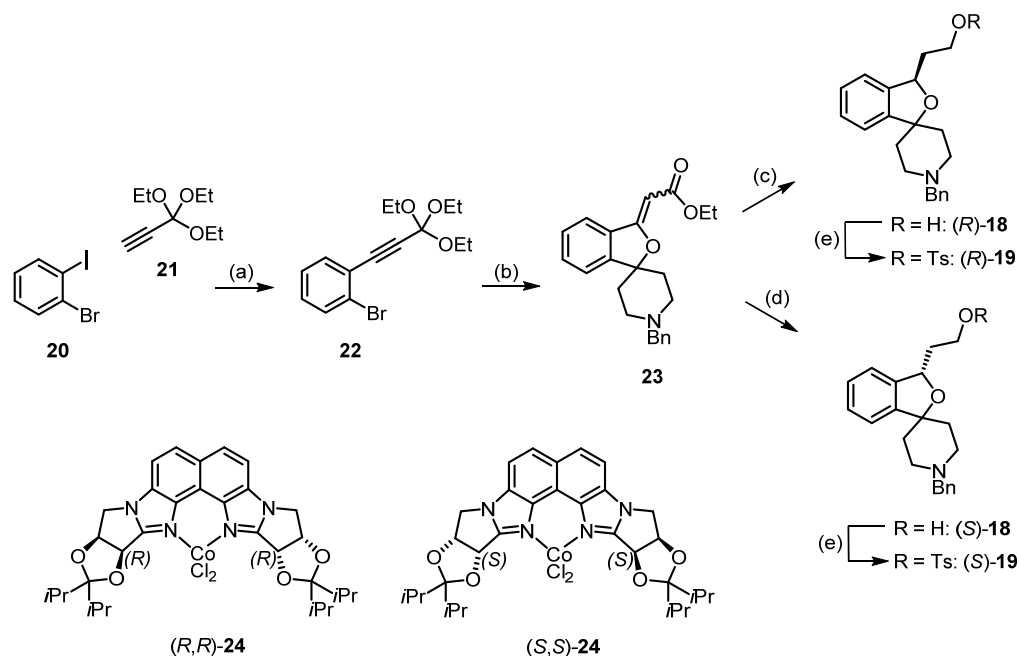
However, the separation of enantiomers inevitably leads to 50% waste, since only one of the enantiomers will be of interest for application as a PET tracer in human studies. Therefore, we developed a novel synthesis method with the enantioselective reduction of a double bond as the key step. Thus, the alkyne **22** was prepared by a Sonogashira reaction of 1-bromo-2-iodobenzene (**20**) with the terminal alkyne **21** bearing an orthoester functional group [37]. Bromine–lithium exchange at **22** and subsequent reaction with 1-benzylpiperidin-4-one directly led to the  $\alpha,\beta$ -unsaturated ester **23**. The best method for the enantioselective reduction of the  $\alpha,\beta$ -unsaturated ester **23** appeared to be the reduction with



$\text{NaBH}_4$  in the presence of chiral co-catalysts (*R,R*)-**24** and (*S,S*)-**24** [38]. The enantiomeric excess was determined after the additional reduction of the ester moiety to a primary alcohol. The reduction of the  $\alpha,\beta$ -unsaturated ester **23** with  $\text{NaBH}_4$  in the presence of (*R,R*)-**24** (0.01 equivalents) led to the alcohol (*R*)-**18** in a 63% yield and 95.6%ee. The enantiomeric co-complex (*S,S*)-**24** (0.01 equivalents) resulted in an 82% yield of (*S*)-**18** and 97.2%ee [39]. Transformation of the primary alcohols (*R*)-**18** and (*S*)-**18** did not change the enantiomeric excess considerably. As the stereocontrol of the co-catalysts (*R,R*)-**24** and (*S,S*)-**24** has been thoroughly investigated, the application in the enantioselective synthesis of both fluspidine enantiomers confirmed the assignment of their absolute configuration by CD-spectroscopy (Scheme 3).



**Scheme 2.** Synthesis of enantiomerically pure fluspidine enantiomers (*R*)-**2** and (*S*)-**2** by chiral resolution of racemic tosylate **19**. Reagents and reaction conditions: (a) Daicel<sup>®</sup> Chiralpak IB, 5  $\mu\text{m}$ , 250 mm/20 mm. Eluent, isohexane:ethanol, 100:2; flow rate, 10.0 mL/min. (*R*)-**19**:  $t_R = 26\text{--}27$  min, 98.2%ee. (*S*)-**19**:  $t_R = 28\text{--}36$  min, 97.8%ee. (b)  $\text{Bu}_4\text{NF}$ , THF, rt, 3.5 h, 69%, 99.6%ee. (c)  $\text{Bu}_4\text{NF}$ , THF, rt, 17 h, 80%, 96.4%ee.



**Scheme 3.** Synthesis of enantiomerically pure alcohols (*R*)-**18** and (*S*)-**18** by enantioselective reduction of  $\alpha,\beta$ -unsaturated ester **23**. Reagents and reaction conditions: (a) Sonogashira coupling— $\text{PdCl}_2(\text{PPh}_3)_2$ ,  $\text{CuI}$ ,  $\text{NEt}_3$ , THF, rt, 15 h, 47%. (b) 1. *n*- $\text{BuLi}$ , THF,  $-78$   $^\circ\text{C}$ ; 2. 1-benzylpiperidin-4-one, 62%. (c) 1.  $\text{NaBH}_4$ , 0.01 equiv. chiral co-complex (*R,R*)-**24**,  $\text{CH}_3\text{OH}/\text{CH}_2\text{Cl}_2$  1:1,  $0$   $^\circ\text{C} \rightarrow$  rt, 30 min; 2.  $\text{LiAlH}_4$ ,  $\text{Et}_2\text{O}$ , yield 63%, 95.6%ee. (d) 1.  $\text{NaBH}_4$ , 0.01 equiv. chiral co-complex (*S,S*)-**24**,  $\text{CH}_3\text{OH}/\text{CH}_2\text{Cl}_2$  1:1,  $0$   $^\circ\text{C} \rightarrow$  rt, 30 min; 2.  $\text{LiAlH}_4$ ,  $\text{Et}_2\text{O}$ , yield 82%, 97.2%ee. (e)  $\text{TsCl}$ ,  $\text{NEt}_3$ , DMAP,  $\text{CH}_2\text{Cl}_2$ , 17 h, (*R*)-**19** (96.2%ee), (*S*)-**19** (96.4%ee).

In an alternative enantioselective synthesis of both fluspidine enantiomers (*R*)-**2** and (*S*)-**2**, (*Z*)-configured methyl 3-silyloxy-3-(2-bromophenyl)acrylate was enantioselectively reduced with the same co-catalysts (*R,R*)-**24**, (*S,S*)-**24** and NaBH<sub>4</sub>. However, the establishment of the spirocyclic framework of fluspidine required six additional reaction steps, starting with a Suzuki coupling [40].

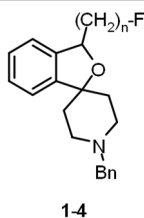
Both enantiomers showed very high  $\sigma_1$  receptor affinity with  $K_i$  values of 0.57 nM for (*R*)-**2** and 2.3 nM for (*S*)-**2**. Moreover, NMDA receptors with a GluN2B subunit and opioid receptors have been determined to have high selectivity over the  $\sigma_2$  subtype.

### 5. In Vitro Characterization of Fluspidine and Its Enantiomers

The lipophilicity of the homologous fluoroalkyl derivatives **1–4** was determined by the micro-shake flask method. After the distribution of the compounds between an *n*-octanol layer and MOPS buffer (pH 7.4), the amount of the compound in the buffer layer was determined by mass spectrometry [41,42]. The recorded  $\log D_{7.4}$  values were compared with the  $\log D_{7.2}$  values determined by the distribution of the analogous <sup>18</sup>F-labeled compounds [<sup>18</sup>F]**1**–[<sup>18</sup>F]**4** between *n*-octanol and phosphate-buffered saline, pH 7.2. The  $\log D_{7.2}$  values were calculated from the distribution of radioactivity in both layers.

In Table 2, the determined  $\log D_{7.4}$  and  $\log D_{7.2}$  values are summarized. As expected, the  $\log D_{7.4}$  and  $\log D_{7.2}$  values increased with the increasing length of the fluoroalkyl side chain from 2.80 (**1**) to 3.71 (**4**) and 2.39 (**1**) to 3.11 (**4**), respectively. The  $\log D_{7.4}$  and  $\log D_{7.2}$  values of all four homologs were in a promising range. It should be emphasized that the  $\log D_{7.4}$  and  $\log D_{7.2}$  values determined by different methods showed a very good correlation [30,32–34].

**Table 2.** Pharmacokinetic properties of spirocyclic piperidines **1–4** with homologous fluoroalkyl side chain.



Compd.	<i>n</i>	$K_i(\sigma_1)$ (nM)	$\log D_{7.4}$ <sup>(a)</sup> Micro Shake Flask	$\log D_{7.2}$ <sup>(b)</sup> PET Tracer	Plasma Protein Binding (%)	In Vitro Metabolism—Intact Compd. after 90 min (%)
<b>1</b>	1	0.74	2.80 ± 0.04	2.39 ± 0.04	84 ± 0.5	53 ± 3.9
<b>2</b>	2	0.59	3.33 ± 0.07	2.57 ± 0.32	88 ± 0.4	34 ± 8.8
<b>3</b>	3	1.4	3.60 ± 0.12	2.78 ± 0.06	91 ± 0.4	33 ± 7.9
<b>4</b>	4	1.2	3.71 ± 0.14	3.11 ± 0.14	95 ± 0.3	28 ± 4.5

<sup>(a)</sup>  $\log D_{7.4}$ : *n*-octanol/MOPS buffer pH 7.4, determined by LC-MS. <sup>(b)</sup>  $\log D_{7.2}$ : *n*-octanol/phosphate buffered saline pH 7.2, determined by measuring the radioactivity in both layers.

Plasma protein binding was recorded by HPLC analysis using a stationary phase coated with human serum albumin. The resulting retention times correlate with binding to human serum albumin [42]. The least lipophilic fluoromethyl derivative **1** exhibited the lowest plasma protein binding (84%), which increased with the increasing length of the fluoroalkyl side chain up to 95% for the fluorobutyl derivative **4** (Table 2).

Metabolic stability was initially determined by microsomal assays involving incubation of the homologous fluoroalkyl derivatives **1–4** with mouse liver microsomes and NADPH. After an incubation period of 90 min, the amount of remaining test compound was determined by LC-MS [42–44]. Under standardized conditions, the metabolic stability decreased with increasing lipophilicity. While the fluoromethyl derivative **1** revealed moderate stability (53% intact after 90 min), the longer homologs **2**, **3** and **4** showed reduced



metabolic stability, with only 34%, 33% and 28% of intact parent compounds **2**, **3** and **4** after 90 min, respectively (Table 2).

The metabolites formed upon incubation of **2**, (*R*)-**2**, and (*S*)-**2** with rat liver microsomes and NADPH were analyzed by LC-MS and MS<sup>n</sup> experiments. Figure 6 shows the formed metabolites. The *N*-debenzylated metabolite **2a** and the *p*-hydroxyphenyl metabolite **2c** represent the main metabolites. The structures of both metabolites were confirmed by independent synthesis. Two metabolites bearing OH moieties in the piperidine ring (**2b**) and the fluoroethyl side chain (**2h**) as well as the *N*-oxide **2d** could be detected. Furthermore, three metabolites **2e–2g** containing two additional O-atoms were detected. Interestingly, the metabolite **2h** with the additional OH moiety in the fluoroethyl side chain was formed only for the (*S*)-configured enantiomer [36].

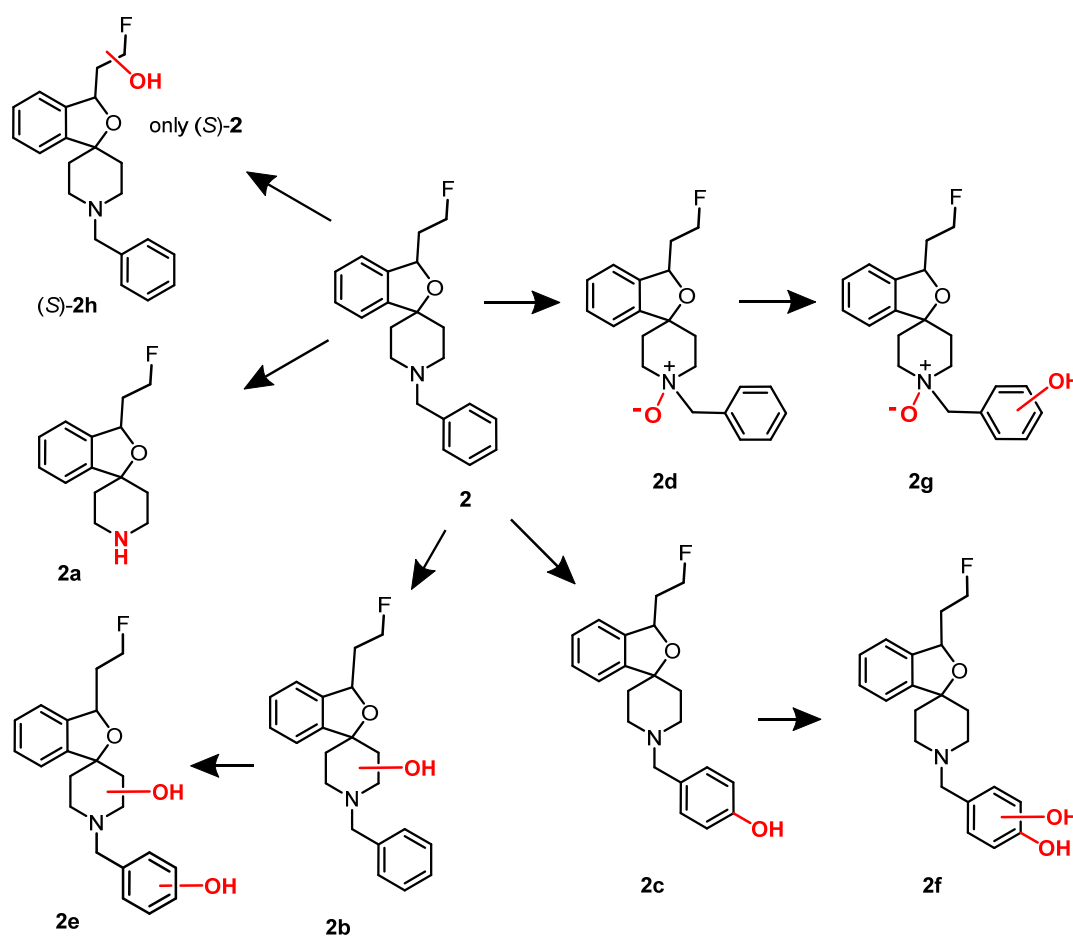


**Figure 6.** Metabolites formed by incubation of **2**, (*R*)-**2**, and (*S*)-**2** with rat liver microsomes and NADPH [36].

## 6. Molecular Interactions of Fluspidine Enantiomers with the $\sigma_1$ Receptor

Molecular dynamics (MD) simulations were employed to elucidate the interactions between the two fluspidine enantiomers (*R*)-**2** and (*S*)-**2** and the  $\sigma_1$  receptor. The X-ray crystal structure 5HK1 [45] of the  $\sigma_1$  receptor from the PDB repository was used for the computational studies. The computational investigation primarily focused on evaluating their binding affinity, examining the patterns of interaction, and assessing potential selectivity based on the orientation of key functional groups. For this purpose, both enantiomers (*R*)-**2** and (*S*)-**2** were modeled and docked into the binding site of the  $\sigma_1$  receptor, and the relevant free energy of binding ( $\Delta G_{\text{bind}}$ ) between the protein and the enantiomers was determined using MM/PBSA calculations [46]. As shown in Figure 7A,B, the analysis of the MD trajectories reveals that both (*R*)-fluspidine and (*S*)-fluspidine bind the  $\sigma_1$  receptor

via the four canonical forms of interactions [9,23,47,48]: (i) a stable salt bridge is established between the positively charged  $R_3NH^+$  group of the piperidine ring of the ligand and the negatively charged  $COO^-$  group of E172. This interaction is facilitated by an optimal arrangement that involves an additional hydrogen bond with Y103. (ii) The aromatic side chain of F107 contributes to the stabilization of the intermolecular complex through a strong  $\pi$ -cation interaction with the aforementioned protonated  $N$ -atom of the ligands. (iii) The analysis also highlights the presence of a robust network of hydrophobic and  $\pi$ - $\pi$  interactions between the benzyl moiety of the fluspidine enantiomers and the aromatic groups of  $\sigma_1$  receptor residues W89, Y120, and W164. These interactions effectively secure the ligand within the protein binding cavity. (iv) Furthermore, several additional hydrophobic interactions contribute to the stability of the ligand/receptor complex. These interactions mainly involve the 2-benzofuran ring and the side chains of the  $\sigma_1$  receptor residues lining the hydrophobic pocket, namely, M93, L105, T181, L182, and T202.

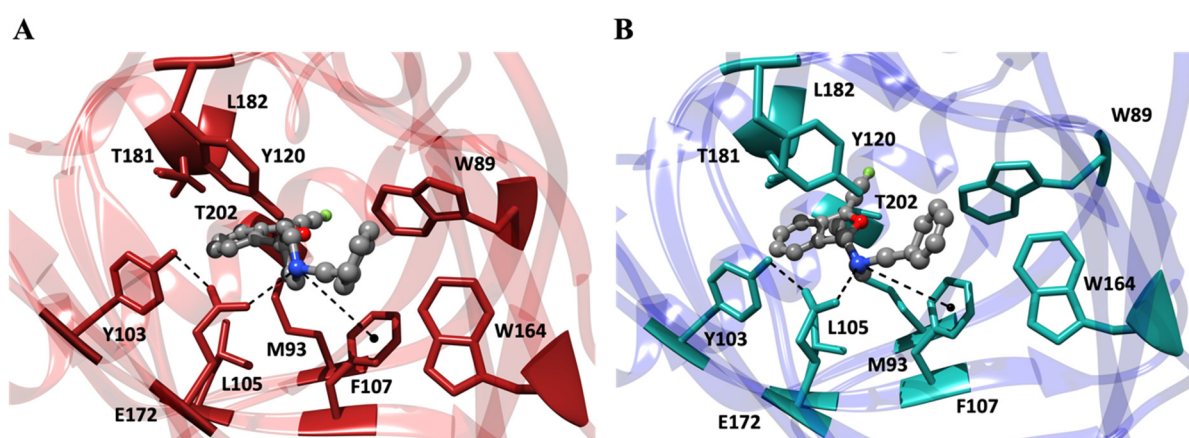


**Figure 7.** Details of (*R*)-fluspidine (**A**) and (*S*)-fluspidine (**B**) in the binding pocket of the  $\sigma_1$  receptor. Compounds are shown as atom-colored sticks-and-balls (C, grey, N, blue, O, red, F, green), while the side chains of the protein residues mainly interacting with the ligands are depicted as colored sticks and labeled. Hydrogen atoms, water molecules, ions, and counterions are omitted for clarity.

In summary, modeling investigations suggest that both enantiomers (*R*)-2 and (*S*)-2 of fluspidine fit well in the binding site of the  $\sigma_1$  receptor by establishing similar stabilizing interactions with the receptor. To quantify these interactions, binding free energy calculations were performed. According to these simulations, the affinities of both enantiomers for the  $\sigma_1$  receptor are comparable. In fact, the receptor exhibits a marginally higher affinity for the (*R*)-configured enantiomer over the (*S*)-enantiomer, as indicated by the corresponding  $\Delta G_{\text{bind}}$  values of  $-11.21 \pm 0.19$  kcal/mol and  $-10.96 \pm 0.21$  kcal/mol, respectively.

To gain further insight into the receptor binding of the two fluspidine enantiomers, the enthalpic component ( $\Delta H_{\text{bind}}$ ) of the binding free energy was decomposed into the contributions provided by the protein residues primarily engaged in each ligand binding. (Figure 8A). The results of this analysis indicate that the significant interaction involving E172 has comparable effects on the stabilization of (*R*)-2 ( $\Sigma\Delta H_{\text{res}} = -4.99$  kcal/mol) and (*S*)-2 ( $\Sigma\Delta H_{\text{res}} = -5.03$  kcal/mol). Additionally, the  $\pi$ -cation interaction with F107 contributes to the stabilization of the (*R*)-2 and (*S*)-2 with comparable  $\Sigma\Delta H_{\text{res}}$  values ( $-2.71$  kcal/mol and  $-2.77$  kcal/mol, respectively). Furthermore, the estimated hydrophobic and  $\pi$ - $\pi$  interactions involving the side chains of residues W89, Y120, and W164 are also almost identical ( $\Sigma\Delta H_{\text{res}} = -4.18$  kcal/mol for (*R*)-2 and  $\Sigma\Delta H_{\text{res}} = -4.15$  kcal/mol for (*S*)-2, respectively), supporting the idea that all the interactions described above almost equally contribute to stabilizing (*R*)-2 and (*S*)-2 in the binding pocket.

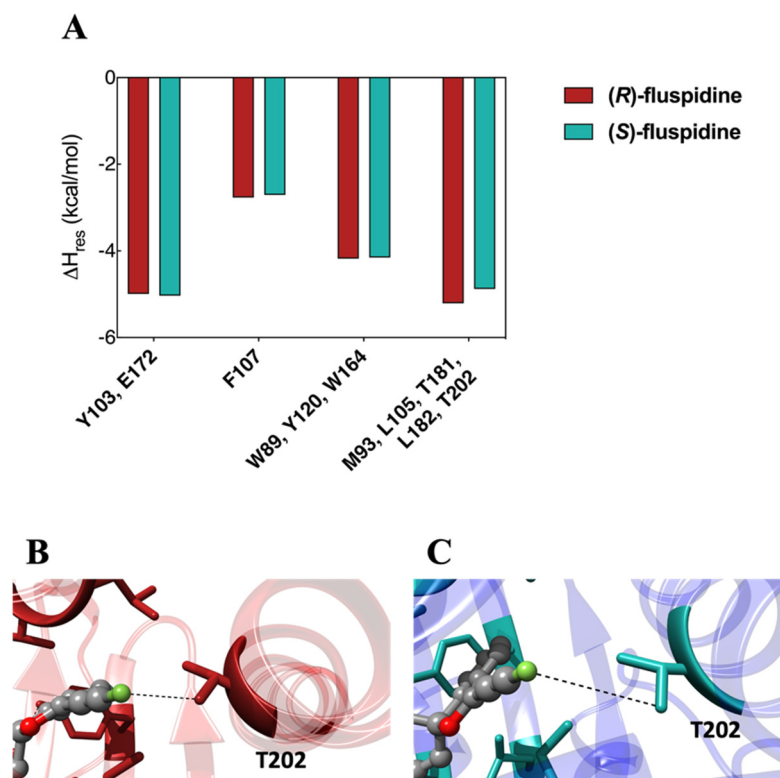


**Figure 8.** (A) Per-residue binding free energy decomposition of the main interacting residues of the  $\sigma_1$ /(*R*)-fluspidine (firebrick) and  $\sigma_1$ /(*S*)-fluspidine (light sea green) complexes. Zoomed details of the interaction between the F-atom and T202 hydroxy group in  $\sigma_1$ /(*R*)-fluspidine (B) and  $\sigma_1$ /(*S*)-fluspidine (C) complexes. Compounds are shown as atom-colored sticks-and-balls (C, grey, N, blue, O, red, F, green).

On the other hand, the marginal disparity in binding affinity of the  $\sigma_1$  receptor for the two fluspidine enantiomers (*R*)-2 and (*S*)-2 can be rationalized by analyzing the stabilizing interactions performed by the ligands in the remaining part of the receptor, that is, the hydrophobic pocket involving residues M93, L105, T181, L182, and T202 (Figure 8B,C), for which the calculated  $\Sigma\Delta H_{\text{res}}$  values are  $-5.21$  kcal/mol and  $-4.88$  kcal/mol for (*R*)-2 and (*S*)-2, respectively.

Beyond these typical hydrophobic interactions, the analysis also revealed that (*R*)-2 exhibits an additional weak electrostatic contact between the fluoroethyl moiety and the hydroxy group of T202. Accordingly, in the case of (*R*)-2, the average dynamic distance (ADD) between these two groups of atoms, as recorded throughout the molecular simulations, is considerably shorter (ADD =  $3.98 \pm 0.12$  Å) compared to that observed for (*S*)-2 (ADD =  $5.15 \pm 0.19$  Å). In conclusion, the structural and energetic evidence provided in this study provides a molecular-based rationale for the slightly higher binding affinity of the  $\sigma_1$  receptor for the (*R*)-configured enantiomer (*R*)-2 of fluspidine.

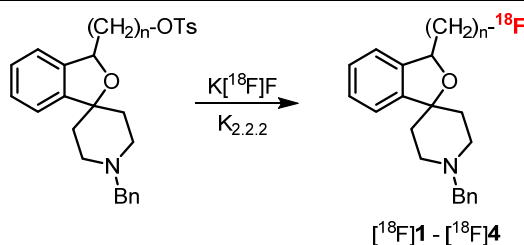
## 7. Radiosynthesis

In nuclear medicine, fluorine-18-labeled PET tracers have emerged as powerful tools for non-invasive molecular imaging. The physical and nuclear properties of fluorine-18 ( $t_{1/2} = 109.8$  min, 97%  $e^+$  ( $\beta^+$ ) decay,  $e^+$  energy 635 keV) [49] and its availability in cyclotron facilities render fluorine-18 superior to other radionuclides. The broad applicability of fluorine-18 was driven by the development of novel radiofluorination methods [50] and the automate-supported production of PET tracers.

The PET tracers [ $^{18}\text{F}$ ]-2–[ $^{18}\text{F}$ ]-4 were prepared by the nucleophilic substitution of the corresponding tosylate precursors with [ $^{18}\text{F}$ ]fluoride. For this purpose, the cryptand  $\text{K}_{2.2.2}$

and  $K_2CO_3$  were added to the aqueous [ $^{18}F$ ]fluoride solution delivered from the cyclotron, followed by the removal of water by azeotropic drying to obtain “naked” and highly nucleophilic [ $^{18}F$ ]fluoride for the radiolabeling step. The PET tracers [ $^{18}F$ ]2–[ $^{18}F$ ]4 were obtained with 35–51% radiochemical yields, high radiochemical purity and high molar activity [32–34] (Table 3). However, the synthesis of the fluoromethyl derivative [ $^{18}F$ ]1 from the corresponding tosylate required the solvent DMSO at 150 °C instead of  $CH_3CN$  at 85 °C. The solvent DMSO and the higher reaction temperature were necessary due to the branched system (2-benzofuran) in the  $\beta$ -position of the tosyloxy moiety. The branch close to the reaction center inhibited the backside attack of the nucleophile [ $^{18}F$ ]fluoride. Under these reaction conditions, the radiochemical yield, radiochemical purity, and molar activity of [ $^{18}F$ ]1 were comparable to those of [ $^{18}F$ ]2–[ $^{18}F$ ]4, while the reaction time was even shorter [30] (Table 3). After the synthesis, PET tracers [ $^{18}F$ ]1–[ $^{18}F$ ]4 were formulated in saline for further investigation and for the first preclinical studies. The total synthesis time was 80–100 min for [ $^{18}F$ ]1 and 90–120 min for [ $^{18}F$ ]2–[ $^{18}F$ ]4.

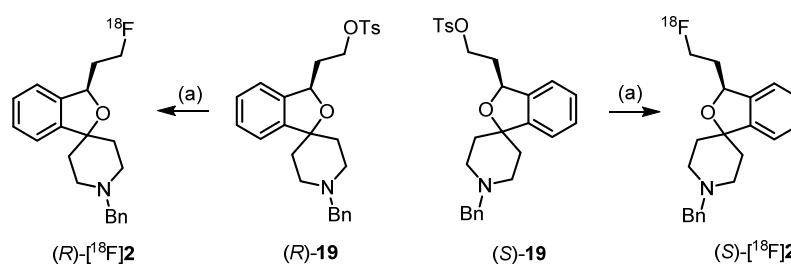
**Table 3.** Radiosynthetic data of the homologous PET tracers [ $^{18}F$ ]1–[ $^{18}F$ ]4 obtained in non-automated synthesis.



PET Tracer	Reaction Conditions (a)	RCY <sub>ni</sub> (b) (%)	RCY <sub>fi</sub> (c) (%)	RCP (d) (%)	A <sub>m</sub> (e) (GBq/μmol)	Time (f) (min)
[ $^{18}F$ ]1 ( <i>n</i> = 1)	DMSO, 150 °C, 10–15 min	67–86 ( <i>N</i> = 4)	38–50 ( <i>N</i> = 3)	>99.1	173–412	80–100
[ $^{18}F$ ]2 ( <i>n</i> = 2)	$CH_3CN$ , 85 °C, 25 min	60–70 ( <i>N</i> = 10)	35–45 ( <i>N</i> = 6)	>99.6	150–350	90–120
[ $^{18}F$ ]3 ( <i>n</i> = 3)	$CH_3CN$ , 85 °C, 30 min	60–70 ( <i>N</i> = 11)	35–48 ( <i>N</i> = 7)	>99.5	150–238	90–120
[ $^{18}F$ ]4 ( <i>n</i> = 4)	$CH_3CN$ , 83 °C, 20 min	60–88 ( <i>N</i> = 8)	45–51 ( <i>N</i> = 7)	>98.6	201–528	90–120

(a) 2.5–3 mg tosylate precursor. (b) RCY<sub>ni</sub>: radiochemical yield (not isolated). (c) RCY<sub>fi</sub>: radiochemical yield (final). (d) RCP: radiochemical purity. (e) A<sub>m</sub>: molar activity. (f) Complete synthesis time until final formulation. Parentheses include the number *N* of experiments.

Since the PET tracers [ $^{18}F$ ]2, (*R*)-[ $^{18}F$ ]2 and (*S*)-[ $^{18}F$ ]2 were set for clinical use, automated syntheses were developed using a TRACERlab FX FN synthesis module. The tosylate precursors **19**, (*R*)-**19** and (*S*)-**19** were reacted with [ $^{18}F$ ]fluoride to obtain the PET tracers [ $^{18}F$ ]2, (*R*)-[ $^{18}F$ ]2 and (*S*)-[ $^{18}F$ ]2 by nucleophilic substitution. After some optimization and adaptation experiments, the PET tracers [ $^{18}F$ ]2, (*R*)-[ $^{18}F$ ]2 and (*S*)-[ $^{18}F$ ]2 were obtained with high radiochemical yields, high radiochemical purity, high molar activity and short reaction times [51,52] (Scheme 4, Table 4).



**Scheme 4.** The automated radiosynthesis of enantiomerically pure fluspidine enantiomers  $(R)\text{-}[^{18}\text{F}]\mathbf{2}$  and  $(S)\text{-}[^{18}\text{F}]\mathbf{2}$ . Reagents and reaction conditions: (a)  $[^{18}\text{F}]\text{KF}$ , Kryptofix-2.2.2, 2.5–3 mg tosylate precursor  $(R)\text{-}\mathbf{19}$  or  $(S)\text{-}\mathbf{19}$ ,  $\text{CH}_3\text{CN}$  (1 mL),  $85^\circ\text{C}$ , 25 min, radiochemical yield (RCY) 35–45% ( $N = 10$ ), radiochemical purity (RCP) > 99.6%, molar activity ( $A_m$ ) 150–350 GBq/ $\mu\text{mol}$ .

**Table 4.** Data obtained in the automated radiosynthesis of the racemic and the enantiomerically pure PET tracers  $[^{18}\text{F}]\mathbf{2}$ ,  $(R)\text{-}[^{18}\text{F}]\mathbf{2}$  and  $(S)\text{-}[^{18}\text{F}]\mathbf{2}$  [51,52].

$[^{18}\text{F}]\mathbf{2}$

PET Tracer	Reaction Conditions (a)	RCY <sub>fi</sub> (b) (%)	RCP (c) (%)	$A_m$ (d) (GBq/ $\mu\text{mol}$ )	Time (e) (min)
$[^{18}\text{F}]\mathbf{2}$	$\text{CH}_3\text{CN}$ , $85^\circ\text{C}$ , 25 min	$37 \pm 8$ ( $N = 9$ )	$99.4 \pm 0.5$ ( $N = 11$ )	$177 \pm 52$ ( $N = 5$ )	$59 \pm 4$ ( $N = 8$ )
$(R)\text{-}[^{18}\text{F}]\mathbf{2}$	$\text{CH}_3\text{CN}$ , $85^\circ\text{C}$ , 15 min	35–45	>99	650–870	70
$(S)\text{-}[^{18}\text{F}]\mathbf{2}$	$\text{CH}_3\text{CN}$ , $85^\circ\text{C}$ , 15 min	35–45	>99	650–870	70

(a)  $\text{K}[^{18}\text{F}]\text{F}$ , K<sub>2.2.2</sub>, 2.5–3 mg tosylate precursor  $\mathbf{19}$ ,  $(R)\text{-}\mathbf{19}$  and  $(S)\text{-}\mathbf{19}$  using the TRACERlab FX FN synthesis module. (b) RCY<sub>fi</sub>: radiochemical yield (final). (c) RCP: radiochemical purity. (d)  $A_m$ : molar activity. (e) Complete synthesis time until final formulation. Parentheses include the number of experiments.

## 8. Preclinical In Vivo Studies of Racemic and Enantiomerically Pure $[^{18}\text{F}]\text{Fluspidine}$ $[^{18}\text{F}]\mathbf{2}$ , $(R)\text{-}[^{18}\text{F}]\mathbf{2}$ and $(S)\text{-}[^{18}\text{F}]\mathbf{2}$

### 8.1. Radiometabolites of $rac\text{-}[^{18}\text{F}]\mathbf{2}$ , $(R)\text{-}[^{18}\text{F}]\mathbf{2}$ and $(S)\text{-}[^{18}\text{F}]\mathbf{2}$ In Vivo

Before detailed preclinical studies were performed using different species, the presence of radiometabolites in the brain was investigated. In the brains of CD-1 mice, 98% of the activity was due to  $rac\text{-}[^{18}\text{F}]\mathbf{2}$  60 min after intravenous administration of the radioligand, indicating the almost complete absence of brain-penetrant radiometabolites [53]. At the same time, the proportion of unchanged PET tracer  $rac\text{-}[^{18}\text{F}]\mathbf{2}$  in mouse plasma was still 75%. In piglets, the metabolisms of the two enantiomers  $(R)\text{-}[^{18}\text{F}]\mathbf{2}$  and  $(S)\text{-}[^{18}\text{F}]\mathbf{2}$  were compared, and plasma samples revealed a higher stability of the  $(S)$ -configured enantiomer [52], although this was lower than in mice (Figure 9). On the contrary,  $(R)\text{-}[^{18}\text{F}]\mathbf{2}$  and  $(S)\text{-}[^{18}\text{F}]\mathbf{2}$  showed comparable fractions of unchanged PET tracer in plasma in rhesus monkeys (>30%, 60 min p.i.) [54], which were in the same range as for  $(S)\text{-}[^{18}\text{F}]\mathbf{2}$  in piglets.

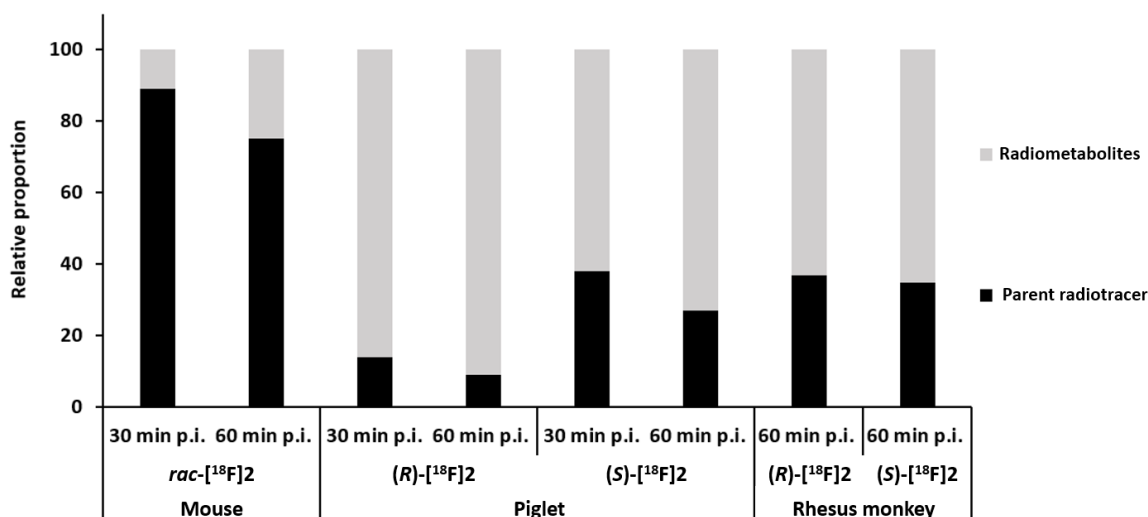


**Figure 9.** Fractions of unchanged PET tracer and radiometabolites in the plasma of various species determined at 30 and 60 min following intravenous administration of the corresponding radioligand [54–61].

8.2. Organ Distribution in Mice, Piglets and Non-Human Primates

The pharmacokinetic properties of *rac*-[<sup>18</sup>F]2 were first investigated by ex vivo organ distribution studies carried out in female CD1-mice [32]. Tissues and organs of interest were isolated at different times after the intravenous (i.v.) administration of the radiotracer to measure the radioactivity. Organ activity time data show a rapid, high and slowly increasing uptake of *rac*-[<sup>18</sup>F]2 in the brain (3.88 and 4.71% of injected dose per g (% ID/g) at 5 and 30 min p.i., respectively), with an activity distribution similar to the immunohistochemical distribution of the  $\sigma_1$  receptor in the mouse brain [55]. The rapid uptake in the brain was followed by a slow washout (2.82% ID/g at 120 min p.i.). The significant reduction in activity uptake after blocking the  $\sigma_1$  receptor by the previous application of haloperidol confirmed the target specificity of *rac*-[<sup>18</sup>F]2 in vivo (Table 5).

**Table 5.** Summary of the distribution pattern of *rac*-[<sup>18</sup>F]2, (S)-[<sup>18</sup>F]2, and (R)-[<sup>18</sup>F]2 binding sites in the brains of mice, piglets and rhesus monkeys.

Species	Parameter (Experimental Details)	Radiotracer	Brain Region (Values)
Mouse [32]	Ratio of activity concentration (target region vs. olfactory bulb at 45 min p.i.; N = 1)	<i>rac</i> -[ <sup>18</sup> F]2	Facial nucleus (4.69), cerebellum (1.75), superficial grey layer of superior colliculus (1.57), cortex (1.45), thalamus (1.24), hippocampus (1.21), striatum (1.11)
		(S)-[ <sup>18</sup> F]2	Midbrain (15.4), colliculi (15.2), cerebellum (14.8), thalamus (14.1), striatum (13.5), hippocampus (13.5), cortex (9.8–13.1)
Piglet [52]	$V_T$ in mL/g (Logan plot; baseline conditions; N = 3)	(R)-[ <sup>18</sup> F]2	Cerebellum (140), midbrain (132), colliculi (123), thalamus (106), striatum (100), hippocampus (95.2), cortex (67.8–98.4)
		(S)-[ <sup>18</sup> F]2	Cortex (14.6–19.6), hippocampus (16.4), putamen (14.9), amygdala (14.6), caudate (13.5), cerebellum (13.6), caudate (13.5), thalamus (12.2)
Rhesus monkey [54]	$V_T$ in mL/g (1-Tissue compartment model; baseline conditions; N = 1)	(R)-[ <sup>18</sup> F]2	Cortex (174–291), putamen (199), hippocampus (193), caudate (181), cerebellum (175), amygdala (153), thalamus (128)



To evaluate the potential use of the  $^{18}\text{F}$ -labelled enantiomers ( $R$ )- $^{18}\text{F}$ 2 and ( $S$ )- $^{18}\text{F}$ 2 for neuroimaging in a large animal model and to establish a modeling method for the accurate quantification of the  $\sigma_1$  receptors in the brain, PET studies were conducted in piglets [52]. These studies showed that both radiotracers ( $R$ )- $^{18}\text{F}$ 2 and ( $S$ )- $^{18}\text{F}$ 2 are rapidly taken up throughout the brain with a standardized uptake value (SUV) of about 2 within 3 min after injection. The specific binding of both radiotracers to the  $\sigma_1$  receptor in the piglet brain was confirmed by the faster brain washout and the reduced activity observed after the blocking of  $\sigma_1$  receptors with SA 4503. Furthermore, the metabolic and brain time–activity curve profiles of both radiotracers indicate the absence of radiometabolites penetrating the blood–brain barrier in the piglets.

However, the differences in the brain uptake kinetics of the two enantiomers in baseline studies indicate that their suitability for diagnostic imaging varies in several pathological situations. Although both enantiomers exhibited similar initial brain uptake, the clearance of ( $R$ )- $^{18}\text{F}$ 2 was noticeably slower than that of ( $S$ )- $^{18}\text{F}$ 2 (SUV<sub>120min p.i.</sub>: ~80% vs. ~50% of SUV<sub>5min p.i.</sub>). Due to the absence of a reference region with no or very low specific uptake in the pig brain, compartmental modeling and graphical analyses were utilized to analyze the dynamic imaging data to obtain measures for the specific binding of both radiotracers. A full, nonlinear kinetic analysis of the baseline scans using metabolite-corrected plasma input function and two-tissue compartment modeling has revealed whole-brain distribution volumes of  $V_T = 13$  and 133 mL/g for ( $S$ )- $^{18}\text{F}$ 2 and ( $R$ )- $^{18}\text{F}$ 2, respectively. Furthermore, data obtained from the Logan plot analysis [56] demonstrate a decrease in  $V_T$  values upon SA 4503's blockade of the  $\sigma_1$  receptors (whole brain ( $S$ )- $^{18}\text{F}$ 2: –55%, ( $R$ )- $^{18}\text{F}$ 2: –89%), confirming the specific binding of both radiotracers.

While the results of the preclinical studies suggest that ( $S$ )- $^{18}\text{F}$ 2 is appropriate for the quantitative neuroimaging of the  $\sigma_1$  receptor and for occupancy evaluations of  $\sigma_1$  receptor-targeting drugs [57], the time–activity curves of ( $R$ )- $^{18}\text{F}$ 2 indicate an apparently irreversible binding to the  $\sigma_1$  receptor. This hypothesis was supported by mouse dosimetry studies [58], PET imaging evaluation in non-human primates [54], and in vitro association and dissociation studies [54], demonstrating the extremely slow washout of ( $R$ )- $^{18}\text{F}$ 2 from the brain in vivo and the negligible dissociation of ( $R$ )- $^{18}\text{F}$ 2 from the binding site in vitro. However, the distribution pattern of ( $R$ )- $^{18}\text{F}$ 2 and the much more rapidly cleared ( $S$ )- $^{18}\text{F}$ 2 in the brain of rhesus monkeys (Table 5) reflect those of other  $\sigma_1$  receptor-specific radiotracers in this species. Finally, the rapid brain uptake kinetics, favorable metabolic profile, and high specific signal observed in studies carried out in non-human primates by Baum et al. [54] confirmed the efficacy of ( $S$ )- $^{18}\text{F}$ 2 in quantifying brain  $\sigma_1$  receptor expression levels.

In a mouse model of glioblastoma multiforma, an increased  $\sigma_1$  receptor density in the tumor was detected with ( $S$ )- $^{18}\text{F}$ 2. An increased  $\sigma_1$  receptor density was also observed during an autoradiographic analysis of samples from patients with glioblastoma using ( $S$ )- $^{18}\text{F}$ 2, confirming the translational relevance of  $\sigma_1$  receptor imaging in oncology [59].

## 9. Human Studies with ( $S$ )- $^{18}\text{F}$ Fluspidine (( $S$ )- $^{18}\text{F}$ 2)

### *Imaging of $\sigma_1$ Receptors in a Clinical Study (Major Depressive Disorder Patients)*

Following preclinical evaluation, the team of Osama Sabri at the Department of Nuclear Medicine of the University of Leipzig, Germany, completed a first-in-man incorporation dosimetry study that initiated successful human PET trials with ( $S$ )- $^{18}\text{F}$ 2 [60]. The objective of this first clinical proof-of-concept study (DRKS00008321) was to test ( $S$ )- $^{18}\text{F}$ 2 in patients with major depressive disorder (MDD) compared to healthy subjects, in accordance with evidence for the antidepressant-like effects of agonistic  $\sigma_1$  receptor ligands [61].

By kinetic modeling using a 1TCM or 2TCM model, the total volume of distribution ( $V_T$ ) of ( $S$ )- $^{18}\text{F}$ 2 can be estimated for all cortical regions from PET 90 min time–activity curves (TACs) with robust and feasible results [62]. Consequently, a PET study with ( $S$ )- $^{18}\text{F}$ 2 is a suitable method for quantifying  $\sigma_1$  receptor availability and related changes in

neuropsychiatric diseases due to its high  $V_T$  and short measurement times. In a study on depression conducted in rats, it was found that MDD rats had decreased levels of cardiac  $\sigma_1$  receptors [63]. Additionally, the genetic inhibition of the  $\sigma_1$  receptor in  $\sigma_1$  knock-out mice led to a depressive-like phenotype [17].

Interestingly, in unmedicated patients with acute early-onset MDD, a PET study with (S)-[ $^{18}\text{F}$ ]2 revealed an increased availability of  $\sigma_1$  receptors in cortico-striato-(para)limbic brain regions compared to healthy volunteers. This increase was strongly correlated with the severity of acute depressive symptoms of MDD and is believed to reflect neuro-adaptive upregulation, which counteracts endoplasmic reticulum (ER) stress [62]. Unfortunately, although the authors of this study suggested additional PET studies with (S)-[ $^{18}\text{F}$ ]2 to investigate  $\sigma_1$  receptor availability in a larger group of patients with depression in different stages of disease and during treatment, it appears that this study has not been planned or performed, leaving a gap in our understanding of the pathophysiology of the  $\sigma_1$  receptor in the context of MDD.

However, during the study mentioned above, the metabolism of (S)-[ $^{18}\text{F}$ ]2 was investigated and a high fraction of unchanged PET tracer (S)-[ $^{18}\text{F}$ ]2 was found in human plasma (see Figure 10) [62,64].

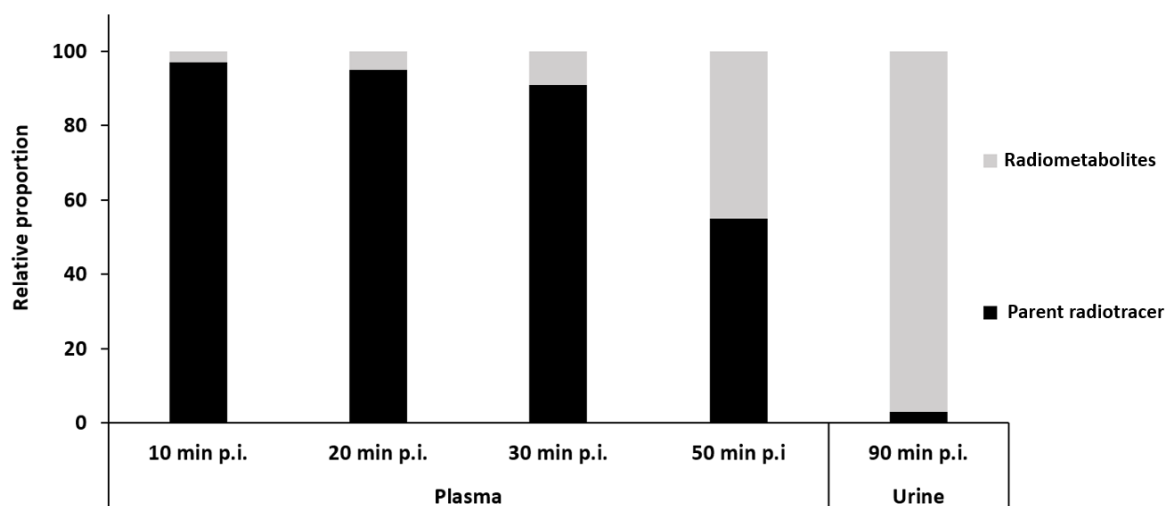


**Figure 10.** Fractions of unchanged PET tracer and radiometabolites in the plasma and urine of humans determined at different times following the intravenous administration of (S)-[ $^{18}\text{F}$ ]2.

In contrast, a high fraction of a single radiometabolite, [ $^{18}\text{F}$ ]2i, and only very small amounts of the unchanged PET tracer (S)-[ $^{18}\text{F}$ ]2 were detected in urine. With the aid of in vitro experiments and LC-MS studies, the structures of the main metabolites were elucidated. The glucuronide [ $^{18}\text{F}$ ]2i represents the main metabolite, which originated from the glucuronidation of the hydroxy metabolite [ $^{18}\text{F}$ ]2h. The secondary amine [ $^{18}\text{F}$ ]2a produced by *N*-debenzylation was detected as a minor metabolite of the PET tracer (S)-[ $^{18}\text{F}$ ]2 (Figure 11).

In addition to non-invasively assessing the expression levels of  $\sigma_1$  receptors subjected to pathological modifications, supporting the evaluation of  $\sigma_1$  receptor as a biomarker for diseases of the CNS, neuroimaging by PET with (S)-[ $^{18}\text{F}$ ]2 allows occupancy studies supporting the development of novel therapeutic drugs. The objective of a corresponding study (NCT03019289), undertaken by Osama Sabri's team, was to demonstrate the target specificity of pridopidine, a drug originally designed for the treatment of CNS pathologies associated with dysfunction of the dopaminergic neurotransmission. Pridopidine (4-[3-(methylsulfonyl)phenyl]-1-propylpiperidine), also known as ACR-16, ASP 2314, FR 310,826 or Huntexil, was originally developed by Arvid Carlsson Research AB as a dopamine stabilizer to reduce hyperactivity and increase behavioral complexity in hypoglutamatergic mice, a model of cognitive deficits in schizophrenia (Figure 12) [65].

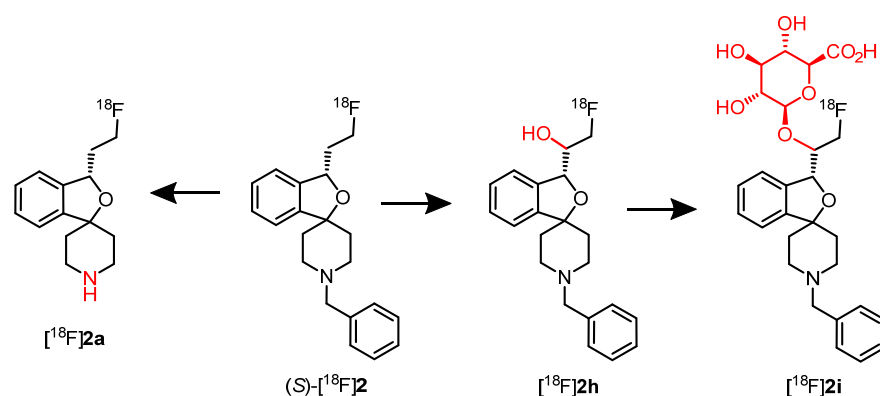


**Figure 11.** Main radiometabolites formed in humans after administration of  $(S)\text{-}[^{18}\text{F}]\mathbf{2}$ .

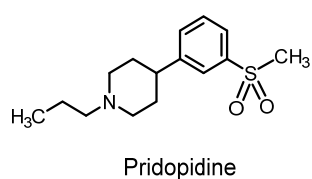


**Figure 12.** Pridopidine interacting with  $\sigma_1$  receptors.

The pharmacological properties of this compound made it an interesting candidate for the treatment of a wide range of neurological and psychiatric disorders, such as L-DOPA-induced dyskinesia associated with levodopa treatment in Parkinson's disease [66–68]. Due to neuroprotective effects observed in models of Huntington's disease (HD) [69], pridopidine was further developed for the treatment of motor symptoms associated with HD. However, different phase 3 studies, initiated by various companies developing pridopidine for clinical applications in HD patients, led to negative results. Therefore, the mechanism of action of pridopidine was reexamined, and a receptor occupancy study in rats indicated the preferential binding of pridopidine to the  $\sigma_1$  receptor compared to dopamine  $D_2$  receptors [69]. In addition, a study in genetically modified mice identified the  $\sigma_1$  receptor as a mediator of pridopidine-induced gene expression in the brain, contributing to the neuromodulatory effects of this drug [70]. These findings suggest that the interaction of pridopidine with the  $\sigma_1$  receptor in humans should be investigated in more detail.

In  $(S)\text{-}[^{18}\text{F}]\mathbf{2}$ , a tool is available that allows the non-invasive evaluation of the occupancy of the  $\sigma_1$  receptor by drugs in the human body using PET [71]. The free fraction in blood plasma of  $(S)\text{-}[^{18}\text{F}]\mathbf{2}$  available for brain uptake has been determined as  $f_p = 0.023$ .  $V_T$  measurements in healthy volunteers confirmed the results of the preclinical studies performed with  $(S)\text{-}[^{18}\text{F}]\mathbf{2}$  in pigs and NHPs discussed above, with values of, e.g., 21 mL/g in the frontal cortex and 19 mL/g in the striatum. The results of the occupancy study using  $(S)\text{-}[^{18}\text{F}]\mathbf{2}$  in a PET study indicated the selective binding of pridopidine to the  $\sigma_1$  receptor in the brains of healthy volunteers and HD patients at therapeutic doses. On the contrary, only minimal occupancy of dopamine  $D_2/D_3$  receptors was found [71].

## 10. Computational Details

The crystal structures of the  $\sigma_1$  receptor were obtained from the available PDB file in the Protein Data Bank repository, 5HK1 [45]. All docking experiments were carried out with Autodock 4.2.6/Autodock Tools1.4 [72] on a win64 platform, following a consolidated procedure [9,47,48]. The resulting docked complexes were solvated with explicit TIP3P [73] water, and then the density and the volume of the system were relaxed in the NPT ensemble, maintaining the Berendsen barostat for 20 ns. After this step, 100 ns of unrestrained NVT production simulation was run for each system. According to this computational recipe,  $\Delta G_{\text{bind}}$  values are calculated for equilibrated structures extracted from the corresponding molecular dynamics (MD) by following the MM/PBSA approach [45]. The per

residue binding free-energy decomposition was performed using the same MD trajectory of each ligand/ $\sigma_1$  complex, with the objective of identifying the key residues involved in the ligand/receptor interaction. This analysis was carried out using the MM/GBSA approach [74], and was based on the same snapshots used in the calculation of the binding free-energy. All simulations were carried out using Amber 21 [75] running on the Marconi100 GPU/CPU supercomputer (CINECA, Bologna, Italy). MarvinSketch was used to draw and display the input chemical structures (Version 23.12.0), ChemAxon Software (<http://www.chemaxon.com>). All images were created in the UCSF Chimera software (version 1.17.3) [76] and the graphs were produced in GraphPad Prism 8 (GraphPad Software, San Diego, CA, USA, [www.graphpad.com](http://www.graphpad.com)).

## 11. Determination of In Vitro Pharmacokinetic Parameters

The pharmacokinetic parameters  $\log D_{7.4}$  value, plasma protein binding and metabolic stability described in Table 2 were determined according to references [41,42].

**Author Contributions:** Conceptualization, B.W.; data in Table 2 were recorded by J.S.; molecular interactions were analyzed and described by E.L. and S.P.; Sections 7–9 were prepared by F.-A.L. and W.D.-C.; writing—review and editing, B.W., F.-A.L., W.D.-C., E.L. and S.P. All authors have read and agreed to the published version of the manuscript.

**Funding:** This work was supported by the Deutsche Forschungsgemeinschaft (DFG), which is gratefully acknowledged. SP and EL acknowledge access to supercomputing resources and financial support from ICSC—Centro Nazionale di Ricerca in high-performance computing, big data, and quantum computing (Spoke 7), WP4 (Pilot applications), T.2.8 (Development and optimization of HPC-based integrated workflows based on flagship codes for personalized (nano)medicine) and CINECA, funded by European Union—NextGenerationEU.

**Conflicts of Interest:** The authors declare no conflicts of interest.

## References

1. Cobos, E.J.; Entrena, J.M.; Nieto, F.R.; Cendan, C.M.; Del Pozo, E. Pharmacology and therapeutic potential of sigma(1) receptor ligands. *Curr. Neuropharmacol.* **2008**, *6*, 344–366. [[CrossRef](#)]
2. Maurice, T.; Su, T.-P. The Pharmacology of Sigma-1 Receptors. *Pharmacol. Ther.* **2009**, *124*, 195–206. [[CrossRef](#)]
3. Smith, S. *Sigma Receptors: Their Role in Disease and as Therapeutic Targets*; Springer: Berlin/Heidelberg, Germany; New York, NY, USA, 2016.
4. Chien, C.C.; Pasternak, G.W. Selective antagonism of opioid analgesia by a sigma system. *J. Pharmacol. Exp. Ther.* **1994**, *271*, 1583–1590.
5. Entrena, J.M.; Cobos, E.J.; Nieto, F.R.; Cendan, C.M.; Gris, G.; Del Pozo, E.; Zamanillo, D.; Baeyens, J.M.  $\sigma_1$  receptors are essential for capsaicin-induced mechanical hypersensitivity: Studies with selective  $\sigma_1$  ligands and  $\sigma_1$  knockout mice. *Pain* **2009**, *143*, 252–261. [[CrossRef](#)]
6. Diaz, J.L.; Cuberes, R.; Berrocal, J.; Contijoch, M.; Christmann, U.; Fernandez, A.; Port, A.; Holenz, J.; Buschmann, H.; Laggner, C.; et al. Synthesis and biological evaluation of the 1-arylpyrazole class of  $\sigma_1$  receptor antagonists: Identification of 4-[2-[5-methyl-1-(naphthalen-2-yl)-1H-pyrazol-3-yloxy]ethyl]morpholine (S1RA, E-52862). *J. Med. Chem.* **2012**, *55*, 8211–8224. [[CrossRef](#)]
7. Wünsch, B. The  $\sigma_1$  receptor antagonist S1RA is a promising candidate for the treatment of neurogenic pain. *J. Med. Chem.* **2012**, *55*, 8209–8210. [[CrossRef](#)]
8. Richelson, E.; Souder, T. Binding of antipsychotic drugs to human brain receptors Focus on newer generation compounds. *Life Sci.* **2000**, *68*, 29–39. [[CrossRef](#)]
9. Blicher, L.; González-Cano, R.; Laurini, E.; Nieto, F.R.; Schmidt, J.; Schepmann, D.; Pricl, S.; Wünsch, B. Conformationally restricted  $\sigma_1$  receptor antagonists from (–)-isopulegol. *J. Med. Chem.* **2023**, *66*, 4999–5020. [[CrossRef](#)]
10. Milenina, L.S.; Krutetskaya, Z.I.K.; Antonov, V.G.; Krutetskaya, N.I. Sigma-1 receptor ligands chlorpromazine and trifluoperazine attenuate  $Ca^{2+}$  responses in rat peritoneal macrophage. *Cell Tissue Biol.* **2022**, *16*, 233–244. [[CrossRef](#)]
11. Ohi, K.; Hashimoto, R.; Yasuda, Y.; Fukumoto, M.; Yamamori, H.; Umeda-Yano, S.; Kamino, K.; Ikezawa, K.; Azechi, M.; Iwase, M.; et al. The SIGMAR1 gene is associated with a risk of schizophrenia and activation of the prefrontal cortex. *Prog. Neuro-Psychopharmacol. Biol. Psych.* **2011**, *35*, 1309–1315. [[CrossRef](#)]
12. Hayashi, T.; Tsai, S.Y.; Mori, T.; Fujimoto, M.; Su, T.P. Targeting ligand-operated chaperone sigma-1 receptors in the treatment of neuropsychiatric disorders. *Expert Opin. Ther. Targets* **2011**, *15*, 557–577. [[CrossRef](#)]
13. Urani, A.; Romieu, P.; Roman, F.J.; Maurice, T. Enhanced antidepressant effect of sigma<sub>1</sub> ( $\sigma_1$ ) receptor agonists in  $\sigma_{25-35}$ -amyloid peptide-treated mice. *Behav. Brain Res.* **2002**, *134*, 239–247. [[CrossRef](#)]

14. Urani, A.; Romieu, P.; Roman, F.J.; Yamada, K.; Noda, Y.; Kamei, H.; Manh Tran, H.; Nagai, T.; Nabeshima, T.; Maurice, T. Enhanced antidepressant efficacy of  $\sigma_1$  receptor agonists in rats after chronic intracerebroventricular infusion of  $\sigma$ -amyloid-(1–40) protein. *Eur. J. Pharmacol.* **2004**, *486*, 151–161. [[CrossRef](#)]
15. Meunier, J.; Ieni, J.; Maurice, T. The anti-amnesic and neuroprotective effects of donepezil against amyloid beta25–35 peptide-induced toxicity in mice involve an interaction with the sigma1 receptor. *Br. J. Pharmacol.* **2006**, *149*, 998–1012. [[CrossRef](#)]
16. Wang, T.; Jia, H. The sigma receptors in Alzheimer's Disease: New potential targets for diagnosis and therapy. *Int. J. Mol. Sci.* **2023**, *24*, 12025. [[CrossRef](#)]
17. Sabino, V.; Cottone, P.; Parylak, S.L.; Steardo, L.; Zorrilla, E.P.  $\sigma_1$  receptor knockout mice display a depressive-like phenotype. *Behav. Brain Res.* **2009**, *198*, 472–476. [[CrossRef](#)]
18. Hayashi, T.; Su, T.P. An update on the development of drugs for neuropsychiatric disorders: Focusing on the  $\sigma_1$  receptor ligand. *Expert. Opin. Ther. Targets* **2008**, *12*, 45–58. [[CrossRef](#)]
19. Lucas, G.; Rymar, V.V.; Sadikot, A.F.; Debonnel, G. Further evidence for an antidepressant potential of the selective  $\sigma_1$  agonist SA 4503: Electrophysiological, morphological and behavioural studies. *Int. J. Neuropsychopharmacol.* **2008**, *11*, 485–495. [[CrossRef](#)]
20. Shirayama, Y.; Nishikawa, T.; Umino, A.; Takahashi, K. p-chlorophenylalanine-reversible reduction of  $\sigma$  binding sites by chronic imipramine treatment in rat brain. *Eur. J. Pharmacol.* **1993**, *237*, 117–126. [[CrossRef](#)]
21. Shirayama, Y.; Nishikawa, T.; Takahashi, K. Differential effects of repeated dl-pentazocine treatment on  $\sigma$  binding sites in discrete brain areas of the rat. *Neurosci. Lett.* **1994**, *165*, 219–222. [[CrossRef](#)]
22. Brust, P.; Deuther-Conrad, W.; Lehmkuhl, K.; Jia, H.; Wünsch, B. Molecular Imaging of  $\sigma_1$  Receptors In Vivo: Current Status and Perspectives. *Curr. Med. Chem.* **2014**, *21*, 35–69. [[CrossRef](#)]
23. Weber, F.; Brust, P.; Laurini, E.; Pricl, S.; Wünsch, B. Fluorinated PET tracers for molecular imaging of  $\sigma_1$  receptors in the central nervous system. In *Sigma Receptors: Their Role in Disease and as Therapeutic Targets*; Advances in Experimental Medicine and Biology; Springer International Publishing: Berlin/Heidelberg, Germany, 2017; Volume 964, pp. 31–48.
24. Xu, R.; Lord, S.A.; Peterson, R.M.; Ferguson-Cantrell, E.A.; Lever, J.R.; Lever, S.Z. Ether modifications to 1-[2-(3,4-dimethoxyphenyl)ethyl]-4-(3-phenylpropyl)piperazine (SA4503): Effects on binding affinity and selectivity for sigma receptors and monoamine transporters. *Bioorg. Med. Chem.* **2015**, *23*, 222–230. [[CrossRef](#)]
25. Matsuno, K.; Senda, T.; Kobayashi, T.; Okamoto, K.; Nakata, K.; Mita, S. SA4503, a novel cognitive enhancer, with sigma 1 receptor agonistic properties. *Behav. Brain Res.* **1997**, *83*, 221–224. [[CrossRef](#)]
26. Ramakrishnan, N.K.; Schepers, M.; Luurtsema, G.; Nyakas, C.J.; Elsinga, P.H.; Ishiwata, K.; Dierckx, R.A.J.O.; van Waarde, A. Cutamesine Overcomes REM Sleep Deprivation-Induced Memory Loss: Relationship to Sigma-1 Receptor Occupancy. *Mol. Imaging Biol.* **2015**, *17*, 364–372. [[CrossRef](#)]
27. Skuza, G. Potential antidepressant activity of sigma ligands. *Pol. J. Pharmacol.* **2003**, *55*, 923–934.
28. Elsinga, P.H.; Kawamura, K.; Kobayashi, T.; Tsukada, H.; Senda, M.; Vaalburg, W.; Ishiwata, K. Synthesis and evaluation of [ $^{18}\text{F}$ ]fluoroethyl SA4503 as a PET ligand for the  $\sigma$  receptor. *Synapse* **2002**, *43*, 259–267. [[CrossRef](#)]
29. Kawamura, K.; Tsukada, H.; Shiba, K.; Tsuji, C.; Harada, N.; Kimura, Y.; Ishiwata, K. Synthesis and evaluation of fluorine-18-labeled SA4503 as a selective  $\sigma_1$  receptor ligand for positron emission tomography. *Nucl. Med. Biol.* **2007**, *34*, 571–577. [[CrossRef](#)]
30. Maisonal, A.; Mastrup, E.G.; Wiese, C.; Hiller, A.; Schepmann, D.; Fischer, S.; Deuther-Conrad, W.; Steinbach, J.; Brust, P.; Wünsch, B. Synthesis, radiofluorination and pharmacological evaluation of a fluoromethyl spirocyclic PET tracer for central  $\sigma_1$  receptors and comparison with fluoroalkyl homologs. *Bioorg. Med. Chem.* **2012**, *20*, 257–269. [[CrossRef](#)]
31. Mastrup, E.G.; Wiese, C.; Schepmann, D.; Brust, P.; Wünsch, B. Synthesis, pharmacological activity and structure affinity relationships of spirocyclic  $\sigma_1$  receptor ligands with a (2-fluoroethyl) residue in 3-position. *Bioorg. Med. Chem.* **2011**, *19*, 393–405. [[CrossRef](#)]
32. Fischer, S.; Wiese, C.; Mastrup, E.G.; Hiller, A.; Deuther-Conrad, W.; Scheunemann, W.; Schepmann, D.; Steinbach, J.; Wünsch, B.; Brust, P. Molecular imaging of  $\sigma$  receptors: Synthesis and evaluation of the potent  $\sigma_1$  selective radioligand [ $^{18}\text{F}$ ]fluspidine. *Eur. J. Nucl. Med. Mol. Imaging* **2011**, *38*, 540–551. [[CrossRef](#)]
33. Große Mastrup, E.; Fischer, S.; Wiese, C.; Schepmann, D.; Hiller, A.; Deuther-Conrad, W.; Steinbach, J.; Wünsch, B.; Brust, P. Evaluation of spirocyclic 3-(3-fluoropropyl)-2-benzofurans as  $\sigma_1$  receptor ligands for neuroimaging with positron emission tomography. *J. Med. Chem.* **2009**, *52*, 6062–6072. [[CrossRef](#)]
34. Maisonal, A.; Mastrup, E.G.; Fischer, S.; Hiller, A.; Scheunemann, M.; Wiese, C.; Schepmann, D.; Steinbach, J.; Deuther-Conrad, W.; Wünsch, B.; et al. A  $^{18}\text{F}$ -labeled fluorobutyl-substituted spirocyclic piperidine derivative as a selective radioligand for PET imaging of sigma<sub>1</sub> receptors. *ChemMedChem* **2011**, *6*, 1401–1410. [[CrossRef](#)]
35. Maier, C.A.; Wünsch, B. Novel  $\sigma$  receptor ligands. part 2. SAR of spiro[[2]benzopyran-1,4'-piperidines] and spiro[[2]benzofuran-1,4'-piperidines] with carbon substituents in position 3. *J. Med. Chem.* **2002**, *45*, 4923–4930. [[CrossRef](#)]
36. Holl, K.; Falck, E.; Köhler, J.; Schepmann, D.; Humpf, H.-U.; Brust, P.; Wünsch, B. Synthesis, characterization, and metabolism studies of fluspidine enantiomers. *Chem. Med. Chem.* **2013**, *12*, 2047–2056. [[CrossRef](#)]
37. Bunse, P.; Würthwein, E.-U.; Wünsch, B. Synthesis of substituted 1-alkylidenephthalanes via lithium-promoted 5-*exo-dig* cyclization. *Eur. J. Org. Chem.* **2018**, 1806–1812. [[CrossRef](#)]
38. Shuto, Y.; Yamamura, T.; Tanaka, S.; Yoshimura, M.; Kitamura, M. Asymmetric NaBH<sub>4</sub>/4-Reduction of C3-Disubstituted 2-Propanoates Catalyzed by a Diamidine Cobalt Complex. *ChemCatChem* **2015**, *7*, 1547–1550. [[CrossRef](#)]



39. Bunse, P.; Schlepfforst, C.; Glorius, F.; Kitamura, M.; Wunsch, B. Short and atom-economic enantioselective synthesis of the  $\sigma_1$  receptor ligands (S)- and (R)-fluspidine—Important tools for positron emission tomography studies. *J. Org. Chem.* **2019**, *84*, 13744–13754. [[CrossRef](#)]
40. Nakane, S.; Yoshinaka, S.; Iwase, S.; Shuto, Y.; Bunse, P.; Wunsch, B.; Tanaka, S.; Kitamura, M. Synthesis of fluspidine via asymmetric  $\text{NaBH}_4$  reduction of silicon enolates of  $\beta$ -keto esters. *Tetrahedron* **2018**, *74*, 5069–5084. [[CrossRef](#)]
41. Galla, F.; Bourgeois, C.; Lehmkuhl, K.; Schepmann, D.; Soeberdt, M.; Lotts, T.; Abels, C.; Ständer, S.; Wunsch, B. Effects of polar  $\kappa$  receptor agonists designed for the periphery on ATP-induced  $\text{Ca}^{2+}$  release from keratinocytes. *Med. Chem. Commun.* **2016**, *7*, 317–326. [[CrossRef](#)]
42. Börgel, F.; Galla, F.; Lehmkuhl, K.; Schepmann, D.; Ametamey, S.M.; Wunsch, B. Pharmacokinetic properties of enantiomerically pure GluN2B selective NMDA receptor antagonists with 3-benzazepine scaffold. *J. Pharm. Biomed. Anal.* **2019**, *172*, 214–222. [[CrossRef](#)]
43. Falck, E.; Begrow, F.; Verspohl, E.; Wunsch, B. In vitro and in vivo biotransformation of WMS-1410, a potent GluN2B selective NMDA receptor antagonist. *J. Pharm. Biomed. Anal.* **2014**, *94*, 36–44. [[CrossRef](#)]
44. Falck, E.; Begrow, F.; Verspohl, E.; Wunsch, B. Metabolism studies of ifenprodil, a potent GluN2B receptor antagonist. *J. Pharm. Biomed. Anal.* **2014**, *88*, 96–105. [[CrossRef](#)]
45. Schmidt, H.R.; Zheng, S.D.; Gurpinar, E.; Koehl, A.; Manglik, A.; Kruse, A.C. Crystal structure of the human  $\sigma_1$  receptor. *Nature* **2016**, *532*, 527. [[CrossRef](#)]
46. Massova, I.; Kollman, P.A. Combined molecular mechanical and continuum solvent approach (MM-PBSA/GBSA) to predict ligand binding. *Perspect. Drug Discov.* **2000**, *18*, 113–135. [[CrossRef](#)]
47. Kopp, N.; Holtschulte, C.; Börgel, F.; Lehmkuhl, K.; Friedland, K.; Civenni, G.; Laurini, E.; Catapano, C.V.; Priel, S.; Humpf, H.-U.; et al. Novel  $\sigma_1$  antagonists designed for tumor therapy: Structure—Activity relationships of aminoethyl substituted cyclohexanes. *Eur. J. Med. Chem.* **2021**, *210*, 112950. [[CrossRef](#)]
48. Holtschulte, C.; Börgel, F.; Westphälinger, S.; Schepmann, D.; Civenni, G.; Laurini, E.; Marson, D.; Catapano, C.V.; Priel, S.; Wunsch, B. Synthesis of Aminoethyl-Substituted Piperidine Derivatives as  $\sigma_1$  Receptor Ligands with Antiproliferative Properties. *ChemMedChem* **2022**, *17*, e202100735. [[CrossRef](#)]
49. Wang, Y.; Lin, Q.; Shi, H.; Cheng, D. Fluorine-18: Radiochemistry and Target-Specific PET Molecular Probes Design. *Front. Chem.* **2022**, *10*, 884517. [[CrossRef](#)]
50. Rong, J.; Haider, A.; Jeppesen, T.E.; Josephson, L.; Liang, S.H. Radiochemistry for positron emission tomography. *Nat. Commun.* **2023**, *14*, 3257. [[CrossRef](#)]
51. Maisonia-Besset, A.; Funke, U.; Wenzel, B.; Fischer, S.; Holl, K.; Wunsch, B.; Steinbach, J.; Brust, P. Automation of the radiosynthesis and purification procedures for [ $^{18}\text{F}$ ]Fluspidine preparation, a new radiotracer for clinical investigations in PET imaging of  $\sigma_1$  receptors in brain. *Appl. Radiat. Isot.* **2014**, *84*, 1–7. [[CrossRef](#)]
52. Brust, P.; Deuther-Conrad, W.; Becker, G.; Patt, M.; Donat, C.K.; Stittsworth, S.; Fischer, S.; Hiller, A.; Wenzel, B.; Dukic-Stefanovic, S.; et al. Distinctive in vivo kinetics of the new  $\sigma_1$  receptor ligands (R)-(+)- and (S)-(–)- $^{18}\text{F}$ -fluspidine in porcine brain. *J. Nucl. Med.* **2014**, *55*, 1730–1736. [[CrossRef](#)]
53. Wiese, C.; Maestrup, E.G.; Galla, F.; Schepmann, D.; Hiller, A.; Fischer, S.; Ludwig, F.-A.; Deuther-Conrad, W.; Donat, C.K.; Brust, P.; et al. Comparison of in silico, electrochemical, in vitro and in vivo metabolism of a homologous series of (radio)fluorinated  $\sigma_1$  receptor ligands designed for positron emission tomography. *ChemMedChem* **2016**, *11*, 2445–2458. [[CrossRef](#)]
54. Baum, E.; Cai, Z.; Bois, F.; Holden, D.; Lin, S.-F.; Lara-Jaime, T.; Kapinos, M.; Chen, Y.; Deuther-Conrad, W.; Fischer, S.; et al. PET imaging evaluation of four  $\sigma_1$  radiotracers in nonhuman primates. *J. Nucl. Med.* **2017**, *58*, 982–988. [[CrossRef](#)] [[PubMed](#)]
55. Phan, V.L.; Urani, A.; Sandillon, F.; Privat, A.; Maurice, T. Preserved sigma1 (sigma1) receptor expression and behavioral efficacy in the aged C57BL/6 mouse. *Neurobiol. Aging.* **2003**, *24*, 865–881. [[CrossRef](#)] [[PubMed](#)]
56. Logan, J.; Fowler, J.S.; Volkow, N.D.; Wolf, A.P.; Dewey, S.L.; Schlyer, D.J.; MacGregor, R.R.; Hitzemann, R.; Bendriem, B.; Gatley, S.J.; et al. Graphical analysis of reversible radioligand binding from time-activity measurements applied to [ $^{11}\text{C}$ -methyl]-(-)-cocaine PET studies in human subjects. *J. Cereb. Blood Flow Metab.* **1990**, *10*, 740–747. [[CrossRef](#)] [[PubMed](#)]
57. Kranz, M.; Sattler, B.; Deuther-Conrad, W.; Fischer, S.; Hiller, A.; Donat, C.; Wunsch, B.; Steinbach, J.; Sabri, O.; Brust, P. Preclinical dose assessment of (S)-(–)-[ $^{18}\text{F}$ ]fluspidine and (R)-(+)-[ $^{18}\text{F}$ ]fluspidine, new PET tracers for imaging of  $\sigma_1$  receptors. *J. Nucl. Med.* **2013**, *54* (Suppl. 2), 1028.
58. Kranz, M.; Sattler, B.; Wüst, N.; Deuther-Conrad, W.; Patt, M.; Meyer, P.M.; Fischer, S.; Donat, C.K.; Wunsch, B.; Hesse, S.; et al. Evaluation of the Enantiomer Specific Biokinetics and Radiation Doses of [ $^{18}\text{F}$ ]Fluspidine—A New Tracer in Clinical Translation for Imaging of  $\sigma_1$  Receptors. *Molecules* **2016**, *21*, 1164. [[CrossRef](#)] [[PubMed](#)]
59. Toussaint, M.; Deuther-Conrad, W.; Kranz, M.; Fischer, S.; Ludwig, F.-A.; Juratli, T.A.; Patt, M.; Wunsch, B.; Schackert, G.; Sabri, O.; et al. Sigma-1 receptor Positron Emission Tomography: A new molecular imaging approach using (S)-(–)-[ $^{18}\text{F}$ ]fluspidine in glioblastoma. *Molecules* **2020**, *25*, 2170. [[CrossRef](#)] [[PubMed](#)]
60. Sattler, B.; Kranz, M.; Wuest, N.; Patt, M.; Meyer, P.; Deuther-Conrad, W.; Fischer, S.; Wunsch, B.; Brust, P.; Sabri, O. First-in-man incorporation dosimetry of (S)-(–)-[ $^{18}\text{F}$ ]fluspidine. *J. Nucl. Med.* **2016**, *57* (Suppl. 2), 1022.
61. Wang, Y.M.; Xia, C.Y.; Jia, H.M.; He, J.; Lian, W.W.; Yan, Y.; Wang, W.P.; Zhang, W.K.; Xu, J.K. Sigma-1 receptor: A potential target for the development of antidepressants. *Neurochem Int.* **2022**, *159*, 105390. [[CrossRef](#)]



62. Meyer, P.; Strauss, M.; Becker, G.; Hesse, S.; Bednasch, K.; Ettrich, B.; Zientek, F.; Rullmann, M.; Wilke, S.; Luthardt, J.; et al. Increased sigma-1 receptor (Sig-1R) binding in the brain of unmedicated patients with acute major depressive disorder (MDD) using the novel Sig-1R-specific radioligand (–)-[<sup>18</sup>F]Fluspidine and PET. *J. Nucl. Med.* **2018**, *59* (Suppl. 1), 551.
63. Guo, Y.; Zhang, C.; Chen, X.; Liu, X.; Ye, T.; Fo, Y.; Shi, S.; Qu, C.; Liang, J.; Shen, B.; et al. Sigma-1 receptor ligands improves ventricular repolarization-related ion remodeling in rats with major depression disorder. *Psychopharmacology* **2021**, *238*, 487–499. [[CrossRef](#)]
64. Ludwig, F.-A.; Fischer, S.; Houska, R.; Hoepfing, A.; Deuther-Conrad, W.; Schepmann, D.; Patt, M.; Meyer, P.M.; Hesse, S.; Becker, G.-A.; et al. In vitro and in vivo Human Metabolism of (S)-[<sup>18</sup>F]Fluspidine—A Radioligand for Imaging  $\sigma_1$  Receptors With Positron Emission Tomography (PET). *Front. Pharmacol.* **2019**, *10*, 534. [[CrossRef](#)] [[PubMed](#)]
65. Carlsson, M.L. Experimental hypoglutamatergia model for cognitive deficits of schizophrenia: Effects of classical neuroleptics, 5-HT 2A receptor blocking antipsychotics, the ampakine CX516 and the dopaminergic stabiliser ACR16. *Eur. Neuropsychopharmacol.* **2002**, *12*, 167–168. [[CrossRef](#)]
66. A. Carlsson Research Ab. New Modulators of Dopamine Neurotransmission. WO/2001/046145; PCT/SE2000/002674, 4 October 2001.
67. Carlsson, M.L.; Carlsson, A.; Nilsson, M. Schizophrenia: From dopamine to glutamate and back. *Curr. Med. Chem.* **2004**, *11*, 267–277. [[CrossRef](#)] [[PubMed](#)]
68. Squitieri, F.; Di Pardo, A.; Favellato, M.; Amico, E.; Maglione, V.; Frati, L. Pridopidine, a dopamine stabilizer, improves motor performance and shows neuroprotective effects in Huntington disease R6/2 mouse model. *J. Cell. Mol. Med.* **2015**, *19*, 2540–2548. [[CrossRef](#)] [[PubMed](#)]
69. Sahlholm, K.; Sijbesma, J.W.; Maas, B.; Kwizera, C.; Marcellino, D.; Ramakrishnan, N.K.; Dierckx, R.A.; Elsinga, P.H.; van Waarde, A. Pridopidine selectively occupies sigma-1 rather than dopamine D2 receptors at behaviorally active doses. *Psychopharmacology* **2015**, *232*, 3443–3453. [[CrossRef](#)] [[PubMed](#)]
70. Dreyman, J.; Geva, M.; Ross, J.; Cha, Y.; Kusko, R.; Escalante-Chong, R.; Zeskind, B.; Laifenfeld, B.; Grossman, I.; Hayden, M. Loss of the Sigma-1 receptor disrupts pridopidine-induced gene expression. *Neurology* **2018**, *90*, P4.048. [[CrossRef](#)]
71. Grachev, I.D.; Meyer, P.M.; Becker, G.A.; Bronzel, M.; Marsteller, D.; Pastino, G.; Voges, O.; Rabinovich, L.; Knebel, H.; Zientek, F.; et al. Sigma-1 and dopamine D2/D3 receptor occupancy of pridopidine in healthy volunteers and patients with Huntington disease: A [<sup>18</sup>F] fluspidine and [<sup>18</sup>F] fallypride PET study. *Eur. J. Nucl. Med. Mol. Imaging* **2021**, *48*, 1103–1115. [[CrossRef](#)] [[PubMed](#)]
72. Morris, G.M.; Huey, R.; Lindstrom, W.; Sanner, M.F.; Belew, R.K.; Goodsell, D.S.; Olson, A.J. AutoDock4 and AutoDockTools4: Automated docking with selective receptor flexibility. *J. Comput. Chem.* **2009**, *30*, 2785–2791. [[CrossRef](#)]
73. Jorgensen, W.L.; Chandrasekhar, J.; Madura, J.D.; Impey, R.W.; Klein, M.L. Comparison of simple potential functions for simulating liquid water. *J. Chem. Phys.* **1983**, *79*, 926–935. [[CrossRef](#)]
74. Onufriev, A.; Bashford, D.; Case, D.A. Modification of the generalized born model suitable for macromolecules. *J. Phys. Chem.* **2000**, *104*, 3712–3720. [[CrossRef](#)]
75. Case, D.A.; Aktulga, H.M.; Belfon, K.; Ben-Shalom, I.Y.; Brozell, S.R.; Cerutti, D.S.; Cheatham, T.E., III; Cisneros, G.A.; Cruzeiro, V.W.D.; Darden, T.A.; et al. *Amber 2021*; University of California: San Francisco, CA, USA, 2021.
76. Pettersen, E.F.; Goddard, T.D.; Huang, C.C.; Couch, G.S.; Greenblatt, D.M.; Meng, E.C.; Ferrin, T.E. UCSF Chimera—A visualization system for exploratory research and analysis. *J. Comput. Chem.* **2004**, *25*, 1605–1612. [[CrossRef](#)]

**Disclaimer/Publisher’s Note:** The statements, opinions and data contained in all publications are solely those of the individual author(s) and contributor(s) and not of MDPI and/or the editor(s). MDPI and/or the editor(s) disclaim responsibility for any injury to people or property resulting from any ideas, methods, instructions or products referred to in the content.